Check for updates

International Journal for Numerical and Analytical Methods in Geomechanics

WILEY

RESEARCH ARTICLE OPEN ACCESS

Evaluation of Soil–Structure Interface Models Considering Cyclic Loading Effect

Hai-Lin Wang[1,2] | Zhen-Yu Yin[2,3] | Xiao-Qiang Gu[1] | Yin-Fu Jin[4]

[1]Department of Geotechnical Engineering, College of Civil Engineering, Tongji University, Shanghai, China | [2]Department of Civil and Environmental Engineering, The Hong Kong Polytechnic University, Hong Kong, China | [3]Research Centre for Resources Engineering towards Carbon Neutrality (RCRE), The Hong Kong Polytechnic University, Hong Kong, China | [4]College of Civil and Transportation Engineering, Shenzhen University, Shenzhen, China

Correspondence: Zhen-Yu Yin (zhenyu.yin@polyu.edu.hk)

Received: 9 May 2024 | **Revised:** 13 July 2024 | **Accepted:** 31 August 2024

Funding: The financial support is provided by the projects (Grants 15217220 and N_PolyU534/20) from the Research Grants Council (RGC) and Research Centre for Resources Engineering towards Carbon Neutrality (RCRE) of The Hong Kong Polytechnic University (Grants No.: 1-BBEM).

Keywords: accumulated normal displacement | constitutive model | cyclic loading | soil–structure interface | stress degradation

ABSTRACT

The simulation of the soil–structure interface (SSI) under cyclic loading is critically important in geotechnical engineering. Numerous studies have been conducted to explore the cyclic behaviors exhibited at the SSI. However, existing model evaluations primarily rely on direct comparisons between experiments and simulations, with limited analysis focused on specific behaviors like accumulated normal displacement and stress degradation under cyclic loading. This study proposes and adapts six SSI models, including three nonlinear incremental models and three elastoplastic models. These models incorporate nonlinear shear modulus, critical state theory, and particle breakage effects to enhance their capability to capture SSI behaviors. Utilizing optimization-based calibration for a fair comparison, the model parameters are fine-tuned based on the experimental data. Comprehensive assessments including global comparisons and specific behaviors like accumulated normal displacement and stress degradation are carried out to evaluate the models' performance. The results indicate that all models effectively replicate the typical behaviors of SSI systems. By incorporating the particle breakage effect, the models can represent both the reversible and irreversible normal displacements under cyclic loading with better performance. The irreversible normal displacement remains stable and is solely influenced by the soil properties rather than the stress level. Moreover, the models successfully capture the stress degradation under constant normal stiffness caused by the irreversible normal displacement.

1 | Introduction

The soil–structure interface (SSI), a thin layer between the soil–structure system, could be critically important for designing geotechnical structures, such as soil anchors, suction caissons, pile foundations, tunnels, and retaining walls. Direct shear tests, simple shear tests, ring torsion shear tests, and annular shear tests are conducted to investigate the cyclic behaviors of the SSI [1–10] Factors that influence the cyclic SSI behaviors such as dilatancy and irreversible normal displacement [8, 11] have been widely investigated, including the interface roughness [7], density [6, 7], tangential displacement amplitude [2, 6, 9], normal stiffness [2, 4, 9, 10], and so forth.

Based on the experiments, complex constitutive models have been developed to capture the cyclic SSI behavior [12–15]. Models such as the Modified Ramberg-Osgood model [16], the exponential model [15, 17], the hypoplastic model [14, 18, 19], and various elastoplastic models [5, 12, 20–28] have been proposed to simulate the cyclic SSI behaviors. The assessment of these models

This is an open access article under the terms of the Creative Commons Attribution License, which permits use, distribution and reproduction in any medium, provided the original work is properly cited.

© 2024 The Author(s). *International Journal for Numerical and Analytical Methods in Geomechanics* published by John Wiley & Sons Ltd.

typically involves direct comparisons between experiments and simulations, ensuring that the models can accurately simulate interface behaviors on a global scale. However, this method lacks specific discussions on behaviors such as accumulated normal displacement or stress degradation during cyclic loading. Consequently, this paper aims to evaluate these frequently recognized interface behaviors under cyclic loading using various interface models and to guide users in selecting an appropriate model in specific conditions.

In this paper, the models are either adopted/enhanced from existing interface models or directly modified from soil models, following the general approach of applying existing soil models to simulate SSI [14, 29]. The simple nonlinear elastic approach and complex elastoplastic approach are both selected for the comparison between these two groups of models. These models include the exponential model proposed by Yang and Yin [15], the hyperbolic model modified from Yang and Yin [15] but uses a hyperbolic function [30], the hypoplastic model modified from Wang et al. [31], the extended modified Cam-Clay (MCC) model proposed by Yang and Yin [32], the SANISAND model modified from Taiebat and Dafalias [33], and the SIMSAND model modified from Yin et al. [34]. Evaluations are conducted on these models to assess their capacity to simulate interface behaviors, including global comparison, stress degradation, and accumulated normal displacement subjected to cyclic loading.

This paper is organized as follows: First, a general framework for the SSI models is introduced; then, six models considering the cyclic loading are briefly presented; next, the models are compared and validated against experimental data, followed by discussions; finally, the conclusions are drawn.

2 | Methodology

2.1 | General Theoretical Framework

A general theoretical framework for SSI modeling is presented to simulate the SSI behaviors. For the sand–structure interface considered here, previous studies usually assumed that the interface thickness lies in the range of 5–14 times the mean particle size of the sand [35, 36]

$$d_s = R_d \times d_{50}, (R_d \approx 5 \sim 14) \tag{1}$$

where d_{50} is the mean particle size, and R_d is a ratio of the interface thickness to the mean particle size. Then the strain can be calculated as follows:

$$\boldsymbol{\varepsilon} = \boldsymbol{u}/d_s \tag{2}$$

where $\boldsymbol{u}$ is the displacement vector. The normal behavior of the SSI is usually described by an elastic spring with stiffness K

$$\mathrm{d}\sigma_n = -K\mathrm{d}u_n = -K'\mathrm{d}\varepsilon_n \tag{3}$$

where d is the differentiation operator, K usually takes the unit of kPa/mm, and $K' = Kd_s$ can be treated as the modified interface stiffness, which takes the same unit as the stress. The SSI tests can be divided into three different types depending on the normal stiffness: constant normal load (CNL, $K = 0$) condition that a constant normal load is applied on the interface; constant normal stiffness (CNS, K = constant, Wernick [37]) condition that the stiffness of the sand–structure interface is a constant; and constant volume (CV, $K = \infty$, Di Donna et al. [38]) condition that the volume of the soil remains a constant and it corresponds to a condition of infinite interface stiffness. In the simulation, the normal stiffness K is usually set to be a very large value to simulate the CV tests.

Similar to a classical soil model, an SSI model should be able to describe the relationship between the stress and strain, except that the SSI model should also consider the normal boundary condition described by Equation (3). The SSI model can be formulated as follows:

$$\begin{aligned}\mathrm{d}\boldsymbol{\sigma} &= \mathbf{D}(\mathrm{d}\boldsymbol{\varepsilon} - \mathrm{d}\boldsymbol{\varepsilon}^p) = \mathbf{D}\mathrm{d}\boldsymbol{\varepsilon}^e = \mathrm{diag}([K_n, G, G])\mathrm{d}\boldsymbol{\varepsilon}^e \\ &= \mathrm{diag}([GR, G, G])\mathrm{d}\boldsymbol{\varepsilon}^e\end{aligned} \tag{4}$$

where $\mathbf{D}$ is the stiffness matrix, R is a ratio of the normal stiffness to the shear modulus, diag is the diagonal matrix operator, $\boldsymbol{\sigma} = [\sigma_n, \tau_s, \tau_t]^\top$ is the stress vector, $\boldsymbol{\varepsilon} = [\varepsilon_n, \gamma_s, \gamma_t]^\top$ is the strain vector, $\boldsymbol{\varepsilon}^e = [\varepsilon_n^e, \gamma_s^e, \gamma_t^e]^\top$, and $\boldsymbol{\varepsilon}^p = [\varepsilon_n^p, \gamma_s^p, \gamma_t^p]^\top$ are the elastic and plastic strain vector. For a nonlinear elastic model such as the hyperbolic model [30], the plastic strain vector is ignored, and the stiffness matrix is assumed to be a nonlinear function of the current stress state

$$\mathrm{d}\boldsymbol{\sigma} = \mathbf{D}(\boldsymbol{\sigma})\mathrm{d}\boldsymbol{\varepsilon} \tag{5}$$

where $\mathbf{D}(\boldsymbol{\sigma})$ is the nonlinear stiffness matrix. For an elastoplastic model such as the MCC model [39], the plastic strain is expressed as

$$\mathrm{d}\boldsymbol{\varepsilon}^p = \mathrm{d}\lambda\frac{\partial g}{\partial \boldsymbol{\sigma}} \tag{6}$$

where $\mathrm{d}\lambda$ is the plastic multiplier, g is the potential function. Considering the consistency condition that guarantees the stress state is always on the yield surface during the loading

$$f(\boldsymbol{\sigma}, \kappa^*) = 0, \quad \mathrm{d}f(\boldsymbol{\sigma}, \kappa^*) = \frac{\partial f}{\partial \boldsymbol{\sigma}}\mathrm{d}\boldsymbol{\sigma} + \frac{\partial f}{\partial \kappa^*}\mathrm{d}\kappa^* = 0 \tag{7}$$

where f is the yield function and κ^* is the hardening variable. For specific SSI boundary conditions, combining Equation (3) and the normal part of the Equation (4) gives

$$\begin{cases}\mathrm{d}\sigma_n = K_n(\mathrm{d}\varepsilon_n - \mathrm{d}\varepsilon_n^p) \\ \mathrm{d}\sigma_n = -K'\mathrm{d}\varepsilon_n\end{cases} \Longrightarrow \mathrm{d}\varepsilon_n = \frac{K_n}{K_n + K'}\mathrm{d}\varepsilon_n^p \tag{8}$$

Substituting Equations (4), (6), and (8) into Equation (7) gives

$$\begin{aligned}\mathrm{d}f(\boldsymbol{\sigma}, \kappa^*) = &\frac{\partial f}{\partial \sigma_n}\frac{K_n K'}{K_n - K'}\mathrm{d}\lambda\frac{\partial g}{\partial \sigma_n} + \frac{\partial f}{\partial \boldsymbol{\tau}}G\left(\mathrm{d}\boldsymbol{\gamma} - \mathrm{d}\lambda\frac{\partial g}{\partial \boldsymbol{\tau}}\right) \\ &+ \frac{\partial f}{\partial \kappa^*}\frac{\partial \kappa^*}{\partial \varepsilon^p}\mathrm{d}\lambda\frac{\partial g}{\partial \boldsymbol{\sigma}} = 0\end{aligned} \tag{9}$$

10969853, 2024, 17, Downloaded from https://onlinelibrary.wiley.com/doi/10.1002/nag.3831 by HONG KONG POLYTECHNIC UNIVERSITY HU NG HOM, Wiley Online Library on [26/11/2024]. See the Terms and Conditions (https://onlinelibrary.wiley.com/terms-and-conditions) on Wiley Online Library for rules of use; OA articles are governed by the applicable Creative Commons License

Then the plastic multiplier $d\lambda$ can be solved as

$$d\lambda = \frac{\frac{\partial f}{\partial \tau} G d\gamma}{\frac{\partial f}{\partial \tau} G \frac{\partial g}{\partial \tau} + \frac{K_n K'}{K_n + K'} \frac{\partial f}{\partial \sigma_n} \frac{\partial g}{\partial \sigma_n} - \frac{\partial f}{\partial \kappa^*} \frac{\partial \kappa^*}{\partial \varepsilon^p} \frac{\partial g}{\partial \sigma}} = \frac{1}{K_p} \frac{\partial f}{\partial \tau} G d\gamma \tag{10}$$

where K_p is the plastic moduli.

2.2 | SSI Models

In this section, six different SSI models are presented, including three nonlinear incremental models and three elastoplastic models.

2.2.1 | Consideration of Some Important Features

The following features are incorporated into all models to improve their ability to capture SSI behaviors, unless specified otherwise.

To introduce the dependency of the stiffness on the soil densities and the stress levels, the equation of the initial shear modulus G suggested by Richart et al. [40] has been adopted

$$G = G_0 \frac{(2.97 - e)^2}{1 + e} \left(\frac{\sigma_n}{P_{at}} \right)^{n_g} \tag{11}$$

where G_0 is the reference shear modulus and n_g is an exponent that usually takes the value of 0.6.

In this study, the following equation of critical state line (CSL) proposed by Yin et al. [41] is used except for the MCC model (it will be introduced in the introduction section of the MCC model)

$$e_c = e_{ref} \exp \left[-\lambda \left(\frac{\sigma_n}{p_{at}} \right)^{\xi} \right] \tag{12}$$

where λ and ξ are two constants controlling the shape of the CSL, p_{at} is the standard atmosphere pressure, and e_{ref} is the reference critical void ratio corresponding to the critical void ratio when the normal stress is zero. According to Yin et al. [34], the density state effect on the stress–displacement strength behavior is implemented into the model by the following equations:

$$\tan \phi_p = \left(\frac{e_c}{e} \right)^{n_p} \tan \phi_c \tag{13}$$

$$\tan \phi_{pt} = \left(\frac{e}{e_c} \right)^{n_d} \tan \phi_c \tag{14}$$

where n_p and n_d are constants to control the degree of density effect in the mobilized strength and stress–dilatancy, and ϕ_c is the critical friction angle. The void ratio e is updated with the following equation:

$$de = -d\varepsilon_n (1 + e_0) \tag{15}$$

where e_0 is the initial void ratio.

Under high-stress levels or a large number of cyclic shear cycles, the particle breakage effect cannot be ignored. For granular materials, due to particle breakage under a high-stress state, the critical void ratio curve tends to move downward in the $e - \ln \sigma_n$ space [42], as shown in the following equation:

$$e_{ref} = e_{refu} + (e_{ref0} - e_{refu}) \exp(-\rho B_r^*) \tag{16}$$

where e_{ref0} and e_{refu} are the initial and ultimate reference critical void ratio, ρ is a constant that controls the decreasing rate of the CSL, and B_r^* is the modified breakage index [43]. A modified energy-based approach is suggested to calculate the breakage index [15, 44]

$$B_r^* = \frac{w^{n_w}}{b + w^{n_w}}, \text{ with } w = \int (\langle \sigma_n d\varepsilon_n \rangle + \tau d\gamma) \tag{17}$$

where $\langle \cdot \rangle$ is the Macaulay brackets, and b, ρ, and n_w are material constants.

2.2.2 | Nonlinear Incremental Models

Nonlinear functions are used to describe the stress–strain relationship for the exponential model [15] and the hyperbolic model [30]

$$\tau = \tan \phi_p \sigma_n [1 - \exp(-a\gamma)] \tag{18}$$

$$\tau = \tan \phi_p \sigma_n [\gamma / (1/a + \gamma)] \tag{19}$$

where ϕ_p is the dynamic peak friction angle, and a is a parameter controlling the rate of nonlinear softening that can be determined by the initial shear modulus G, and it can be calculated by the following equation for both models

$$G = \left. \frac{d\tau}{d\gamma} \right|_{\gamma=0} \Longrightarrow a = \frac{G}{\tan \phi_p \sigma_n} \tag{20}$$

Differentiating Equations (18) and (19) with respect to γ gives

$$\frac{d\tau}{d\gamma} = G(1 - \eta / \tan \phi_p) + \frac{K_n K'}{K_n + K'} A_d (\tan \phi_{pt} - \eta) [\eta - a\gamma (\tan \phi_p - \eta)] \tag{21}$$

$$\frac{d\tau}{d\gamma} = G(1 - \eta / \tan \phi_p)[a/(a + \gamma)] + \frac{K_n K'}{K_n + K'} A_d (\tan \phi_{pt} - \eta) [\eta - a\eta/(a + \gamma)] \tag{22}$$

where $\eta = \tau / \sigma_n$ is the stress ratio, A_d is a dilatancy parameter, and ϕ_{pt} is the mobilized phase transformation friction angle to introduce the effect of the stress–dilatancy. A modified stress–dilatancy relation of Roscoe and Burland [39] by Yin and Chang [45] is adopted in this paper

$$\frac{d\varepsilon_n^{in}}{d\gamma} = A_d (\tan \phi_{pt} - \eta) \tag{23}$$

where $d\varepsilon_n^{in}$ is the induced normal strain that is similar to the induced elastoplastic normal strain. By incorporating a similar

10969853, 2024, 17, Downloaded from https://onlinelibrary.wiley.com/doi/10.1002/nag.3831 by HONG KONG POLYTECHNIC UNIVERSITY HU NG HOM, Wiley Online Library on [26/11/2024]. See the Terms and Conditions (https://onlinelibrary.wiley.com/terms-and-conditions) on Wiley Online Library for rules of use; OA articles are governed by the applicable Creative Commons License

stress–strain relation to the interface normal behavior as the one used in elastoplastic models, the normal strain increment can be calculated as

$$\mathrm{d}\sigma_n = K_n\left(\mathrm{d}\varepsilon_n - \mathrm{d}\varepsilon_n^{in}\right) \Longrightarrow \frac{\mathrm{d}\varepsilon_n}{\mathrm{d}\gamma} = \frac{K_n}{K_n + K'} A_d(\tan\phi_{pt} - \eta) \quad (24)$$

Similar to the hypoplastic interface model proposed by Stutz et al. [14, 18], the hypoplastic model modified from Wang et al. [31] adopted a unified nonlinear function to describe the stress–strain relationship by introducing additional coefficients to the basic hypoplastic model to consider the nonlinear shear modulus, the critical state theory, and the particle breakage effect. The stress–strain relationship can be described as

$$\mathrm{d}\boldsymbol{\sigma} = I_{se}\left[c_1\sigma_n \mathrm{d}\boldsymbol{\varepsilon} + c_2 \mathrm{d}\varepsilon_n \boldsymbol{\sigma} + c_3 \frac{\sum(\boldsymbol{\sigma}\mathrm{d}\boldsymbol{\varepsilon})}{\sigma_n}\boldsymbol{\sigma} + c_4(\boldsymbol{\sigma} + \boldsymbol{s})\|\mathrm{d}\boldsymbol{\varepsilon}\| I_e\right] \quad (25)$$

where $\boldsymbol{s} = [0, \tau_s, \tau_t]^\top$ is the shear stress vector; $I_{se} = (e_c/e)^{n_p}$ and $I_e = (e/e_c)^{n_d}$ are the critical state function and stiffness function, respectively; c_1, c_2, c_3, and c_4 are constants that can be determined by simple one-way CV experiments

$$\mathrm{d}\tau_s\Big|_{\gamma_s=0} = 0 \Longrightarrow c_1\sigma_{n0}I_{se0} = G \quad (26)$$

$$\mathrm{d}\tau_s\Big|_{\gamma_s\to\infty} = 0 \Longrightarrow c_1 + c_3\mu^2 + 2c_4|\mu| = 0 \quad (27)$$

and one-way CNL experiments

$$\mathrm{d}\sigma_n|_{\gamma_s=0} = 0 \Longrightarrow (c_1 + c_2 + c_3)\nu_i + c_4\sqrt{1+\nu_i^2}I_{e0} = 0 \quad (28)$$

$$\mathrm{d}\sigma_n|_{\gamma_s\to\infty} = 0 \Longrightarrow (c_1 + c_2 + c_3)\nu_f + c_4\sqrt{1+\nu_f^2} + c_3\mu = 0 \quad (29)$$

where $\nu = \mathrm{d}\varepsilon_n/\mathrm{d}\gamma_s$, $\nu_f = 0$, and $\mu = \tan\phi_c = \eta_s|_{\gamma_s\to\infty}$. The coefficients c_1, c_2, c_3, and c_4 can be solved by combining Equations (26)–(29)

$$c_1 = G/(\sigma_{n0}I_{se0}), c_2 = c_1\left[\sqrt{1+\nu_i^2}I_{e0}/\mu\nu_i - \left(1 + 1/\mu^2\right)\right],$$
$$c_3 = c_1/\mu^2, c_4 = -c_1/\mu \quad (30)$$

The normal strain increment can be solved by combining Equation (3) and the first component of Equation (25), and the shear modulus can be solved directly by the second component of Equation (25)

$$\frac{\mathrm{d}\varepsilon_n}{\mathrm{d}\gamma_s} = -\frac{d_1d_2 + d_3\sqrt{{d_1}^2 + d_4{d_2}^2 - d_4{d_3}^2}}{{d_2}^2 - {d_3}^2} \quad (31)$$

$$\frac{\mathrm{d}\tau_s}{\mathrm{d}\gamma_s} = I_{se}\left[c_1\sigma_n + c_2\tau_s\nu + c_3\tau_s(\nu + \eta_s + \eta_t\cdot n) + 2c_4\tau_s I_e\sqrt{1+\nu^2+n^2}\frac{|\mathrm{d}\gamma_s|}{\mathrm{d}\gamma_s}\right] \quad (32)$$

where $n = \mathrm{d}\gamma_t/\mathrm{d}\gamma_s$, $d_1 = c_3I_{se}(\tau_s + \tau_t\cdot n)$, $d_2 = -K' + \sigma_n(c_1 + c_2 + c_3)I_{se}$, $d_3 = c_4\sigma_nI_eI_{se}$, and $d_4 = 1 + n^2$. Assuming the normal strain $\mathrm{d}\varepsilon_n$ in $\|\mathrm{d}\boldsymbol{\varepsilon}\|$ can be ignored, the equation of the normal displacement can be simplified as

$$\mathrm{d}\varepsilon_n = \frac{K_n'}{K_n' + K'}A_d'(\tan\phi_{pt} - \eta)\mathrm{d}\gamma \quad (33)$$

where $K_n' = (c_1 + c_2 + c_3)\sigma_nI_{se}$, $A_d' = \frac{\nu_i}{\mu\sqrt{1+\nu_i^2}I_{e0}I_{se}}$ which is very similar to the normal stiffness of soil K_n and dilatancy parameter A_d.

Table 1 shows the summary of equations for three different nonlinear incremental models.

2.2.3 | Elastoplastic Models

The extended MCC model proposed by Yang and Yin [32] uses a general yield surface that can be applied to both sand and clay, combined with the MCC yield surface [39] and the yield surface for crushing surface of sand [46]

$$f = \frac{1}{n}\left(\frac{\eta}{\tan\phi_p - m\eta}\right)^{n+1}\sigma_n + \sigma_n - \sigma_{ci}(1+\chi) \quad (34)$$

where m and n are constants, σ_{ci} represents the size of the intrinsic yield surface, and χ is the bounding ratio with an initial value of χ_0. The yield surface of the extended MCC model is an irregular ellipse shown in Figure 1. The degree of irregularity is determined by the parameters m and n, where m determines the size of the yield surface in the normal stress direction, and n determines the skewness of the yield surface. For the case of $m = 0, n = 1$, the yield surface is identical to the MCC model.

The model adopts a nonassociated flow rule by the following potential function

$$g = \frac{1}{n}\left(\frac{\eta}{\tan\phi_{pt}}\right)^{n+1}\sigma_n + \sigma_n - \sigma_{ci}(1+\chi) \quad (35)$$

The hardening rules of χ and σ_{ci} are

$$\mathrm{d}\chi = -\xi_c\chi\sqrt{\mathrm{d}\varepsilon_i^p\mathrm{d}\varepsilon_i^p}, \quad \mathrm{d}\sigma_{ci} = \sigma_{ci}\frac{1+e_0}{\lambda-\kappa}\mathrm{d}\varepsilon_n^p \quad (36)$$

where ξ_c is a hardening parameter that controls the effect of the bounding ratio. By introducing the bounding surface concept, the plastic moduli in Equation (10) become the plastic moduli of the bounding surface ($\overline{K_p}$), and the plastic moduli of the current yield surface can be calculated by

$$K_p = \left\{1 + h_p[(\lambda-\kappa)\ln(\mathrm{OCR})]^2\mathrm{OCR}^{|\tan\phi-\eta|}\right\}\overline{K_p}$$
$$\mathrm{OCR} = \frac{\sigma_{ci}(1+\chi)}{\sigma_{cd}}, \quad \sigma_{\mathrm{cd}} = \frac{1}{n}\left(\frac{\eta}{\tan\phi - m\eta}\right)^{n+1}\sigma_n + \sigma_n \quad (37)$$

where h_p is a hardening parameter that controls the effect of the over-consolidation, and κ is related to the normal stiffness

$$K_n = \frac{1+e_0}{\kappa}\sigma_n \quad (38)$$

10969853, 2024, 17, Downloaded from https://onlinelibrary.wiley.com/doi/10.1002/nag.3831 by HONG KONG POLYTECHNIC UNIVERSITY HU NG HOM, Wiley Online Library on [26/11/2024]. See the Terms and Conditions (https://onlinelibrary.wiley.com/terms-and-conditions) on Wiley Online Library for rules of use; OA articles are governed by the applicable Creative Commons License

TABLE 1 | Summary of nonlinear incremental models.

Model	Equations and notes	Reference
Exponential	$\mathrm{d}\tau = G\left(1-\eta/\tan\phi_p\right)\mathrm{d}\gamma + \frac{K_n K'}{K_n - K'} A_d\left(\tan\phi_{pt}-\eta\right)\left[\eta - a\gamma\left(\tan\phi_p-\eta\right)\right]\mathrm{d}\gamma$	Equation 21
	$\mathrm{d}\varepsilon_n = \frac{K_n}{K_n - K'} A_d(\tan\phi_{pt}-\eta)\mathrm{d}\gamma$	Equation 24
	Features: nonlinear shear modulus (11), critical state line (12), particle breakage (16), proposed by Yang and Yin [15]	
Hyperbolic	$\mathrm{d}\tau = G\left(1-\eta/\tan\phi_p\right)\left[a/(a+\gamma)\right]\mathrm{d}\gamma + \frac{K_n K'}{K_n - K'} A_d\left(\tan\phi_{pt}-\eta\right)\left[\eta - a\eta/(a+\gamma)\right]\mathrm{d}\gamma$	Equation 22
	$\mathrm{d}\varepsilon_n = \frac{K_n}{K_n - K'} A_d(\tan\phi_{pt}-\eta)\mathrm{d}\gamma$	Equation 24
	Features: nonlinear shear modulus (11), critical state line (12), particle breakage (16), modified from Yang et al. [15] with a hyperbolic function [30]	
Hypoplastic	$\mathrm{d}\tau = I_{se}\left[c_1\sigma_n + c_2\tau_s\nu + c_3\tau_s\left(\nu+\eta_s+\eta_t\cdot n\right) + 2c_4\tau_s I_e\sqrt{1+\nu^2+n^2}\frac{\lvert\mathrm{d}\gamma_s\rvert}{\mathrm{d}\gamma_s}\right]\mathrm{d}\gamma$	Equation 32
	$\mathrm{d}\varepsilon_n = \frac{K_n'}{K_n' + K'} A_d'(\tan\phi_{pt}-\eta)\mathrm{d}\gamma$	Equation 33
	Features: nonlinear shear modulus (11), critical state line (12), particle breakage (16), modified from Wang et al. [31]	

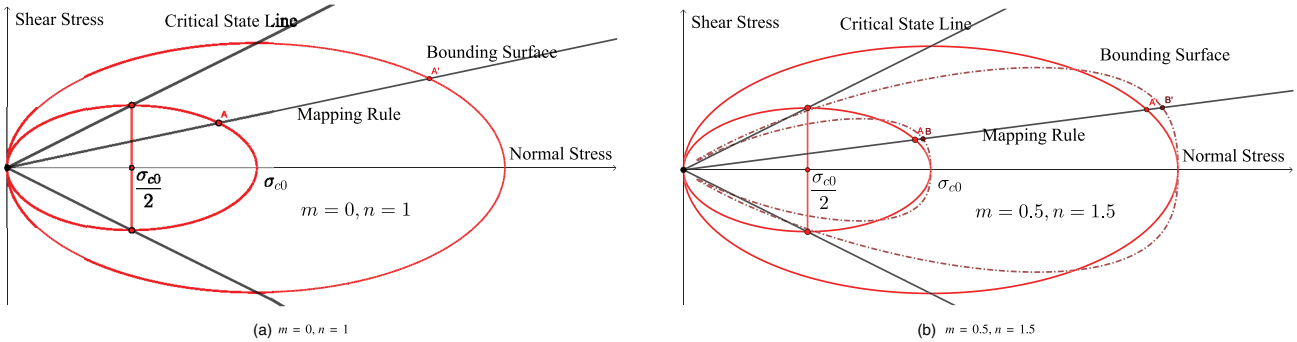

FIGURE 1 | Yield surface of the extended MCC model: (a) $m = 0, n = 1$; (b) $m = 0.5, n = 1.5$. MCC, modified Cam-Clay.

The CSL of the extended MCC model is represented by

$$e_c = e_{ref} - \lambda \log \sigma_n \tag{39}$$

where λ is a model parameter.

The SANISAND model is directly modified from the corresponding soil model [33] similar to the SANISAND interface model proposed by Staubach et al. [29], and the SIMSAND model is directly modified from the corresponding soil model [34], except that the interface features are incorporated into the model. Moreover, to be consistent with other models, the nonlinear shear modulus shown in Equation (11) and the CSL shown in Equation (12) are also used in the SANISAND and SIMSAND SSI models. Table 2 summarizes the elastoplastic SSI models.

2.2.4 | Summary of Model Parameters

Table 3 shows the required parameters for different SSI models.

2.3 | Modeling Technique for Cyclic Loading

The above equations only apply to monotonic loading. When the direction of the shear strain changes (i.e., the dot product of the current shear strain and the last shear strain is less than zero, $\mathrm{d}\boldsymbol{\gamma}_{i-1}\cdot\mathrm{d}\boldsymbol{\gamma}_i < 0$), the stress–strain relationship needs to be modified.

2.3.1 | Stress Reversal Method for Exponential, Hyperbolic, and SIMSAND Models

Figure 2 shows the stress reversal method used in exponential, hyperbolic, and SIMSAND models. In these three models, the amplitude of the shear stress ratio is determined by the peak friction angle ϕ_p ($\tan\phi_p = (e_c/e)^{n_p}\tan\phi_c$) shown in Equation (13), which describes the distance between the initial state and the critical state. Under monotonic loading, the shear stress ratio η lies in the range of 0 to $\tan\phi_p$, and it will finally converge to $\tan\phi_c$ which lies on the CSL. When the direction of the shear displacement changes, the initial state of the unloading process becomes the reversal point, thus the amplitude of the shear stress ratio should be scaled according to the distance between the reversal state and the CSL

$$\tan\phi_p^* = \lVert \tan\phi_p \cdot \mathbf{n} - \boldsymbol{\eta}^R \rVert \tag{40}$$

$$\tan\phi_{pt}^* = \lVert \tan\phi_{pt} \cdot \mathbf{n} - \boldsymbol{\eta}^R \rVert \tag{41}$$

10969853, 2024, 17, Downloaded from https://onlinelibrary.wiley.com/doi/10.1002/nag.3831 by HONG KONG POLYTECHNIC UNIVERSITY HU NG HOM, Wiley Online Library on [26/11/2024]. See the Terms and Conditions (https://onlinelibrary.wiley.com/terms-and-conditions) on Wiley Online Library for rules of use; OA articles are governed by the applicable Creative Commons License

TABLE 2 | Summary of elastoplastic models.

Model	Category	Equations and notes	Reference
MCC	Yield surface	$f = \frac{1}{n}\left(\frac{\eta}{\tan\phi_p - m\eta}\right)^{n+1}(\sigma_n + \sigma_b) + \sigma_n - \sigma_{ci}(1+\chi)$	Equation 34
	Flow rule	$g = \frac{1}{n}\left(\frac{\eta}{\tan\phi_{pt}}\right)^{n+1}(\sigma_n + \sigma_b) + \sigma_n - \sigma_{ci}(1+\chi)$	Equation 35
	Hardening rules	$d\chi = -\xi_c\chi\sqrt{d\varepsilon_i^p d\varepsilon_i^p}, \quad d\sigma_{ci} = \sigma_{ci}\frac{1+e_0}{\lambda-\kappa}d\varepsilon_n^p$	Equation 36
	Note	Features: nonlinear shear modulus (11), critical state line (39), proposed by Yang and Yin [32]	
SANISAND	Yield surface	$f = (\tau - \sigma_n\alpha)^2 - m^2\sigma_n^2\left[1 - \left(\frac{\sigma_n}{p_0}\right)^n\right]$	Taiebat et al. [33]
	Flow rule	$d\sigma_n = \|\boldsymbol{\eta} - \boldsymbol{\alpha}\|A_d\|\boldsymbol{\alpha}^{\boldsymbol{d}} - \boldsymbol{\alpha}\|d\lambda,\ d\tau = (\eta - \alpha)d\lambda$	
	Hardening rules	$d\varepsilon_n = \left(Dr_{ef} + e^{-Vr_{ef}}\right)d\lambda,\ d\boldsymbol{\gamma} = \left(sr_{ef} + X\boldsymbol{\eta}e^{-Vr_{ef}}\right)d\lambda$ $d\alpha = d\lambda h(\eta - \alpha)(\alpha^b - \alpha)$ $dp_0 = \frac{(1+e)p_0 e^{-Vr_{ef}}}{e\left[\rho_c - (p_0/p_{at})^{1/3}/K_0\,(1 - \mathrm{sgn}\delta\lvert\delta\rvert^{\theta})\right]}$	
	Note	Features: nonlinear shear modulus (11), critical state line (12), particle breakage (16), modified from Taiebat et al. [33]	
SIMSAND	Yield surface	$f = \eta - \frac{\tan\phi_p\|\boldsymbol{\gamma}^{\boldsymbol{p}}\|}{k_p + \|\boldsymbol{\gamma}^{\boldsymbol{p}}\|}$	Yin et al. [34]
	Flow rule	$d\sigma_n = A_d\left(\tan\phi_{pt} - \eta\right)d\lambda,\ d\tau = \eta d\lambda$	
	Hardening rules	$d\varepsilon_n = A_d\left(\tan\phi_{pt} - \eta\right)d\lambda,\ d\boldsymbol{\gamma} = \frac{\boldsymbol{\gamma}^{\boldsymbol{p}}}{\|\boldsymbol{\gamma}^{\boldsymbol{p}}\|}d\lambda,\ \frac{\partial\|\boldsymbol{\gamma}^{\boldsymbol{p}}\|}{\partial\boldsymbol{\gamma}^{\boldsymbol{p}}} = \frac{\boldsymbol{\gamma}^{\boldsymbol{p}}}{\|\boldsymbol{\gamma}^{\boldsymbol{p}}\|}$	
	Note	Features: nonlinear shear modulus (11), critical state line (12), particle breakage (16), modified from Yin et al. [34]	

Abbreviation: MCC, modified Cam-Clay.

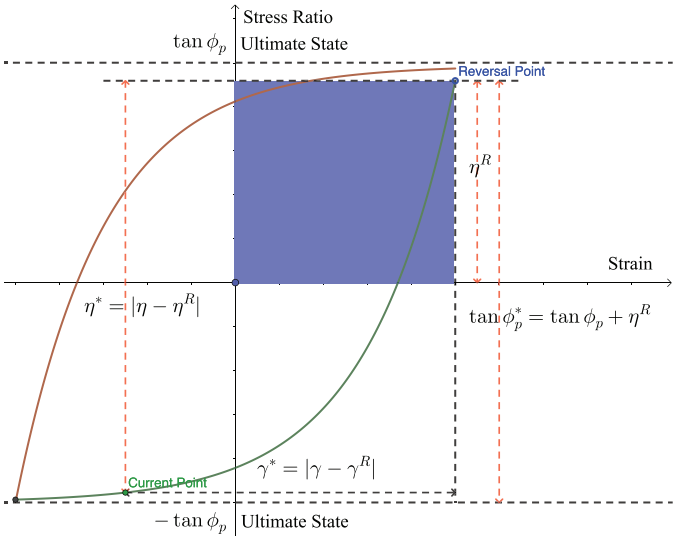

FIGURE 2 | Stress reversal method used in exponential, hyperbolic, and SIMSAND models.

where $\mathbf{n} = \boldsymbol{\gamma}/\|\boldsymbol{\gamma}\|$ is a vector representing the direction of the shear strain in two directions, $\|\cdot\|$ is the norm of the vector, and $\boldsymbol{\eta}^R$ is the shear stress ratio at the reversal state.

2.3.2 | Bounding Surface Method for SANISAND and MCC Models

Figure 3 shows the bounding surface theory used in the SANISAND model [33]. When the stress reversal occurs in $\eta = \alpha + m$ (shown in the green point in the yield surface in Figure 3), according to the hardening rule of the rotation index α (assume the bounding stress ratio in extension α_e^b equals the bounding stress ratio in compression α_c^b)

$$d\alpha \propto \frac{\eta - \alpha}{\alpha^b - \alpha} \tag{42}$$

where b_0 is a model constant, α^b is the bounding stress ratio which is always positive, and α is the rotation index which can be

10969853, 2024, 17, Downloaded from https://onlinelibrary.wiley.com/doi/10.1002/nag.3831 by HONG KONG POLYTECHNIC UNIVERSITY HU NG HOM, Wiley Online Library on [26/11/2024]. See the Terms and Conditions (https://onlinelibrary.wiley.com/terms-and-conditions) on Wiley Online Library for rules of use; OA articles are governed by the applicable Creative Commons License

TABLE 3 | Parameters of the SSI models required.

Category	Symbol	Description	Models
Thickness	d_{50}	Mean particle size	All models
	R_d	Ratio of the thickness of the sand layer to the median particle size	All models
Void ratio	e_0	Initial void ratio	All models
Elastic stiffness	G_0	Reference shear modulus	All models
	n_g	An exponent in the equation of nonlinear shear modulus	All models
	R	Ratio of the elastic normal modulus to the elastic shear modulus	Except hypoplastic
CSL	ϕ_c	Critical friction angle	All models
	e_{ref0}	Reference critical void ratio	All models
	λ	A constant that controls the shape of the critical state line	All models
	ξ	A constant that controls the shape of the critical state line	Except MCC
	n_p, n_d	Constants that control the effect of the density of the soil on the hardening/softening behaviors of the interface	Except MCC
Breakage	e_{refu}	Ultimate reference critical void ratio	Except MCC
	ρ	A constant controls the decreasing rate of CSL	All models
	b, n_w	Constants control the effect of the energy on the breakage index	All models
Dilatancy	A_d	A constant that controls the effect of the dilatancy	Except hypoplastic, MCC
	ν_i	Initial dilatancy slope in the hypoplastic model, $(\mathrm{d}\varepsilon_n/\mathrm{d}\gamma)\|_{\gamma=0}$	Hypoplastic
Yield surface	m, n	Constants that control the shape of the yield surface	MCC, SANISAND
	k_p	A constant that controls the shape of the yield surface	SIMSAND
	σ_{c0}	Initial size of yield surface in MCC	MCC
Hardening	χ_0, ξ_c	Initial bounding ratio and a parameter for bounding ratio	MCC
	h_p	A hardening parameter to control the effect of over-consolidation	MCC
	h_0, c_h	Stress-ratio-related hardening parameters	SANISAND

Abbreviations: CSL, critical state line; MCC, modified Cam-Clay.

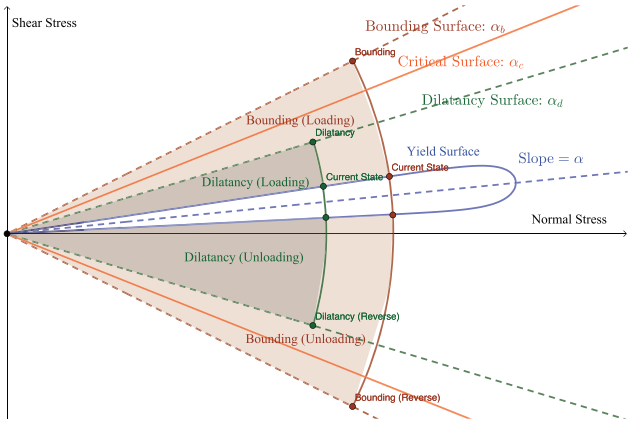

FIGURE 3 | Bounding surface theory.

positive or negative. Item $\alpha^b - \alpha$ measures the distance between the current yield surface and the bounding surface in extension or compression (the narrowness of the yield surface guarantees that the current state is very close to the bisector of the yield surface). During unloading, $\eta - \alpha = -m < 0$ will induce the rotation index α to decrease, and simultaneously, the yield surface will move towards the bounding surface. Similarly, the normal stress–strain behavior is affected by the dilatancy surfaces, shown in the brown point in the yield surface in Figure 3 (the current state is different from the previous state just for demonstration). It can be seen that the stress reversal method used in exponential, hyperbolic, and SIMSAND models is very similar to the bounding surface theory ($\tan\phi_p$ and $\tan\phi_{pt}$ are just like the bounding surface and the dilatancy), except that the stress reversal method used in exponential, hyperbolic, and SIMSAND models is more simple and can be easily implemented in the simple nonlinear SSI models.

Unlike the SANISAND model, the yield surface of the MCC model zooms instead of rotating during the shearing process. Because of the symmetrical yield surface and the CSL shown in Figure 1, under cyclic loading, the stress state of the soil always changes between two CSLs.

2.3.3 | Hypoplastic Model

A unified nonlinear equation is used in the hypoplastic model during loading and unloading, except that the final stress state changes along with the loading/unloading process, specifically

10969853, 2024, 17, Downloaded from https://onlinelibrary.wiley.com/doi/10.1002/nag.3831 by HONG KONG POLYTECHNIC UNIVERSITY HU NG HOM, Wiley Online Library on [26/11/2024]. See the Terms and Conditions (https://onlinelibrary.wiley.com/terms-and-conditions) on Wiley Online Library for rules of use; OA articles are governed by the applicable Creative Commons License

TABLE 4 | Detailed information on the experiments.

Name Unit	N	d_{50} (mm)	BC	Stiffness (kN/mm)	Normal stress (kPa)	Void ratio	Relative density	Amplitude (mm)	Cycles	Reference
Hostun	4	0.47	CNL	0	100	0.66	90%	0.4/0.5/0.7/1.0	4	[12]
Gravel-Zhang	2	10	CNL	0	200/700	0.486	—	40	20	[47]
Crushed quartz	2	0.6	CNL/CNS	0/400	100/300	0.70	88%	0.60/0.65	55	[48]

Abbreviation: CNS, constant normal stiffness.

determined by the nonlinear term in the constitutive equation. Equation (27) guarantees that the final stress state lies on the CSL with the slope of $\mu = \pm \tan\phi_c$. During loading, $\mu = \tan\phi_c = \eta_s|_{\gamma_s \to \infty}$, and Equation (27) guarantees that the final shear stress ratio η_s converges to the slope of the CSL $\tan\phi_c$, whereas it converges to $-\tan\phi_c$ during unloading. Moreover, the introduction of the critical state function I_e helps to introduce the concept of the void ratio in the critical state concept to consider the effect of the density of the soil which is similar to other models.

3 | Model Evaluations

3.1 | Introduction of the Experiments

The performance of the SSI models is examined by experiments under different conditions. Experiments conducted by Shahrour and Rezaie [12], Zhang and Zhang [47], and Fakharian [48] are used to validate the proposed models. Detailed information on the experiments is listed in Table 4. The experiments by Shahrour and Rezaie [12] were conducted on a silica sand and a steel block with sand grains glued at its surface. The experiments by Zhang and Zhang [47] were conducted using the TsingHua-20 tonne Cyclic Shear Apparatus for Soil–Structure Interface (TH-20t CSASSI) on a conglomerate grave with a dry density of 1.75 g/cm^3 and a steel plate with different roughnesses. The experiments by Fakharian [48] were conducted with direct shear test apparatus on a crushed quartz with the minimum void ratio of 0.651 and maximum void ratio of 1.024 and a 2-mm thick aluminum plate. Other properties of the experiments are listed in Table 4.

3.2 | Calibration of the Model Parameters

The SSI models require the identification of several parameters to be used in the simulations. Some parameters can be tested directly before the experiments, such as the mean particle size d_{50} and the initial void ratio e_0; some parameters can be identified by the experiment data, such as the critical friction angle ϕ_c, which is the slope of the CSL; and some other parameters cannot be identified from the experiments since they are coupled with other parameters and cannot be determined individually.

To identify the model parameters in a unified way for a fair comparison, an optimization-based parameter identification method is used to find the best-fitted model parameters for the experiments. Assuming $\mathbf{Y}_{\text{obs}}$ represents the observed experiment data, and $\mathbf{Y}_{\text{pre}}(\mathbf{X})$ represents the predicted data by the analytical model, where $\mathbf{X}$ is the model parameters, model calibration is then the process to minimize the difference between the observed data and the predicted data

$$\mathbf{X} = \arg\min_{\mathbf{X}} \left\{ \text{dist}\left[\mathbf{Y}_{\text{obs}}, \mathbf{Y}_{\text{pre}}(\mathbf{X})\right] \right\} \tag{43}$$

where dist(·) is a function to describe the distance between $\mathbf{Y}_{\text{obs}}$ and $\mathbf{Y}_{\text{pre}}(\mathbf{X})$; it is usually defined as the root mean square error (RMSE) of the relative difference:

$$\text{dist}\left[\mathbf{Y}_{\text{obs}}, \mathbf{Y}_{\text{pre}}(\mathbf{X})\right] = \sum_{i=1}^{m} l_i \sqrt{\frac{1}{n}\sum_{j=1}^{n}\left[\frac{\mathbf{Y}_{\text{pre},ij}(\mathbf{X}) - \mathbf{Y}_{\text{obs},ij}}{\text{T}\left(\mathbf{Y}_{\text{obs},i}\right)}\right]^2} \tag{44}$$

where $\text{T}\left(\mathbf{Y}_{\text{obs},i}\right)$ represents the range of observations, i represents different types of experiments or test variables, j represents different measured points of a certain variable in a single experiment, and l_i is the weights of different variables or experiments. This study uses the CMA-ES (covariance matrix adaption evolution strategy) algorithm [49] to conduct the model calibration.

Table 5 shows the identified model parameters for the experiments based on the optimization method. The results show that all the models are able to simulate the experiments with satisfactory accuracy where the RMSE of the relative difference is less than 12%.

3.3 | Results of the Model Evaluations

3.3.1 | Hostun Sand–Steel Experiments: A General Comparison

The Hostun sand (silica)–steel interface experiments are performed using a modified direct shear box test under different cyclic displacement amplitudes by Shahrour and Rezaie [12]. Four constant normal load experiments with the initial normal stress $\sigma_{n0} = 100$ kPa and the cyclic amplitudes of 0.4, 0.5, 0.7, and 1.0 mm are conducted.

Figure 4 shows the comparison between the experiments and simulations for the Hostun sand–steel interface experiments.

It can be seen that in general, all models can successfully simulate the experiments with satisfaction. For the normal displacement, the interface shows contractive behavior at each reversal point followed by dilative behavior. Despite the high relative density of 90%, the soil exhibits a considerable contractive normal displacement. This phenomenon can be attributed to particle breakage, and it will be discussed in the following section. Additionally, at large cyclic amplitudes, the irreversible normal

10969853, 2024, 17, Downloaded from https://onlinelibrary.wiley.com/doi/10.1002/nag.3831 by HONG KONG POLYTECHNIC UNIVERSITY HU NG HOM, Wiley Online Library on [26/11/2024]. See the Terms and Conditions (https://onlinelibrary.wiley.com/terms-and-conditions) on Wiley Online Library for rules of use; OA articles are governed by the applicable Creative Commons License

TABLE 5 | Identified model parameters for the experiments.

	Exponential			Hyperbolic			Hypoplastic			MCC			SANISAND			SIMSAND		
Parameters	**CQ**	**GZ**	**HOS**	**CQ**	**GZ**	**HOS**	**CQ**	**GZ**	**HOS**	**CQ**	**GZ**	**HOS**	**CQ**	**GZ**	**HOS**	**CQ**	**GZ**	**HOS**
R_d	7.6	4.6	5.5	15.8	4.8	3.1	5.7	8.9	5.4	5.2	20.4	17.4	6	4.7	3	3	4.6	8.7
ϕ	26.1	33.5	27.3	35.4	35.1	23.7	28.3	34.4	28.7	31.9	42.5	30.5	30.3	38.3	44	43.8	39.1	38.2
G_0	1345	405	2624	4218	782	1879	350	916	1643	832	1513	15656	786	391	1546	2559	584	5179
A_d	1.15	0.4	0.41	0.57	0.32	0.48							1.33	0.83	1.16	0.38	0.44	0.93
R	0.57	1.98	1.41	0.45	3.02	8.56				9.15	3.04	0.01	1.52	3.1	8.73	0.11	2.85	6.75
λ	0.01	0.03	0	0.79	0.01	0.61	0.1	0.04	0.12	0.05	0.05	0.04	0.26	0.17	0.13	0.48	0	0.03
ξ	4.55	1.3	4.17	0.06	1.82	4.94	2.11	0.7	5				0	0.53	0.96	1.16	1.25	2.21
e_{ref0}	2.21	1.48	0.67	1.58	0.7	1.2	1.71	0.67	6.91				1.59	1.38	0.98	1.16	0.44	0.69
n_p	0.23	0.14	20	1.28	1.16	20	1.62	9.56	19.62	0	0	0.98	0.34	0.06	2.09	0.15	0	2.75
n_d	0.05	0.04	11.55	3.45	0.43	2.18	0.22	0.51	0.16	0.13	0	0.65	0.01	0.13	5.24	0.2	0.24	19.1
ρ	15.44	9.83	3.68	3.96	5.86	11.78	3.77	15.73	176.96				170.21	17.21	386.08	27.55	18.21	54.01
e_{refu}	0	0.1	0.01	0.16	0.05	0.36	0.69	0.32	3.53				0.03	0.1	0.49	0	0.02	0.68
b	12,556	9590	71,522	28,094	19,456	270,699	7924	13,052	6801				11,906	10,243	1290	10,430	10,296	528
n_w	0.97	0.8	2	1.09	0.89	2	1.42	0.79	0.41				0.55	0.71	0.11	0.85	0.71	1.31
v_i							0.49	0.19	0.29									
ξ_c										80	100	63						
χ_0										1011	6	0						
h_p										142	34	25						
n										1.33	2	1.03						
m										0.25	0.49	0.1						
h_0													0.03	0.07	0.03			
k_p																0.06	0.05	0.003
RMSE (%)	4.30	10.90	11.50	5.40	11.50	11.00	6.40	11.70	11.90	6.00	10.10	11.20	4.90	10.30	12.00	5.50	10.70	11.60

Abbreviations: MCC, modified Cam-Clay; RMSE, root mean square error.

10969853, 2024, 17, Downloaded from https://onlinelibrary.wiley.com/doi/10.1002/nag.3831 by HONG KONG POLYTECHNIC UNIVERSITY HU NG HOM, Wiley Online Library on [26/11/2024]. See the Terms and Conditions (https://onlinelibrary.wiley.com/terms-and-conditions) on Wiley Online Library for rules of use; OA articles are governed by the applicable Creative Commons License

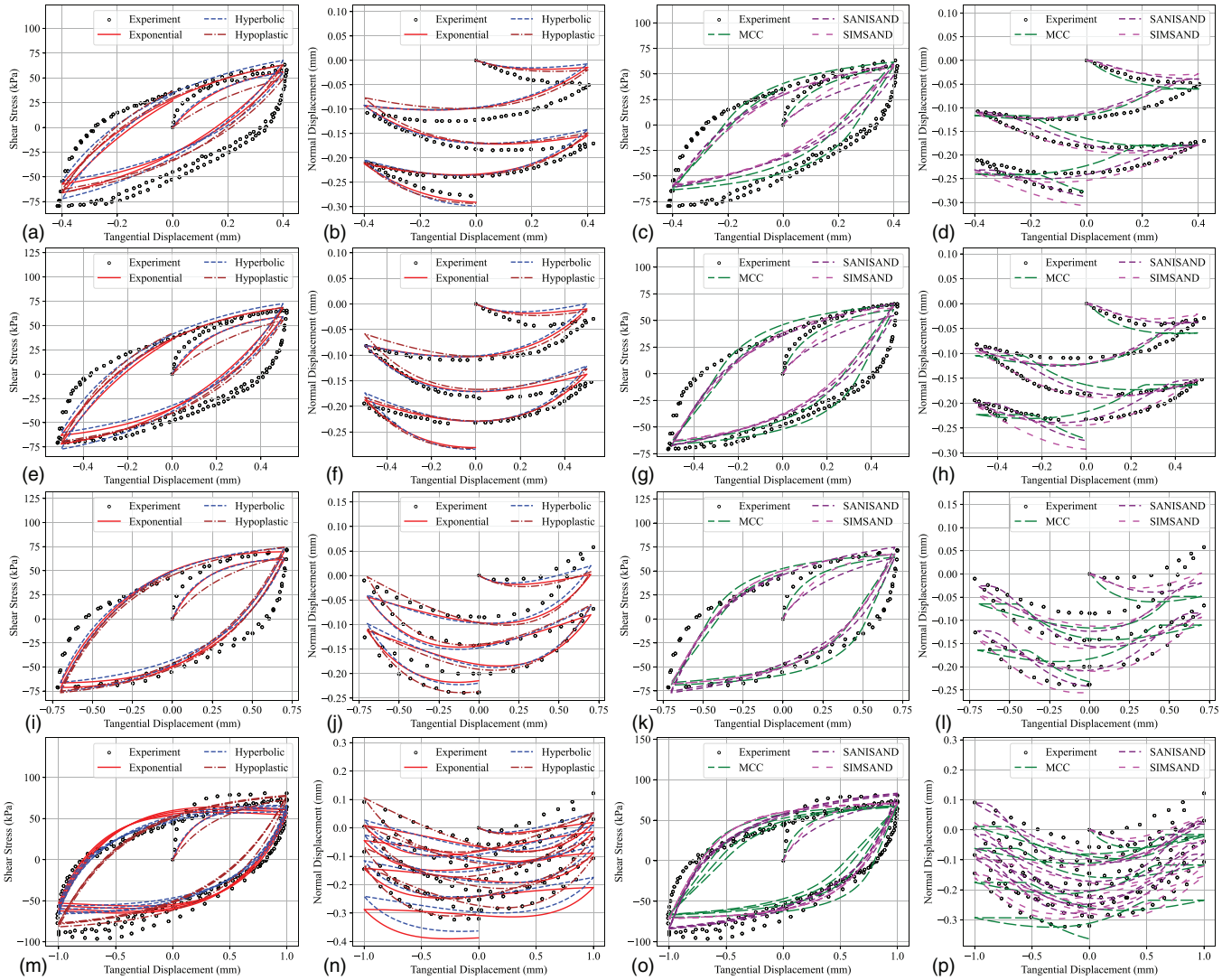

FIGURE 4 | Comparison between the experiments and simulations for the Hostun sand–steel experiments: (a)–(d) shear stress and normal displacement for nonlinear incremental and elastoplastic models with amplitude of 0.4 mm; (e)–(h) shear stress and normal displacement for nonlinear incremental and elastoplastic models with amplitude of 0.5 mm; (i)–(l) shear stress and normal displacement for nonlinear incremental and elastoplastic models with amplitude of 0.7 mm; (m)–(p) shear stress and normal displacement for nonlinear incremental and elastoplastic models with amplitude of 1.0 mm.

displacement exhibits a declining trend, which can be ascribed to the dilative behavior of the interface. However, the shear stress remains relatively constant across different cyclic amplitudes, which can be attributed to the unique nature of the critical state. The interface reaches the critical state even at the lowest cyclic amplitude.

3.3.2 | Conglomerate Gravel–Steel Experiments: Irreversible Normal Displacement

The conglomerate gravel–steel experiments are performed using a direct shear test by Zhang and Zhang [47]. The experiments are conducted under the initial normal stress of 200 and 700 kPa with the constant normal load condition and the cyclic amplitude of 40 mm.

Figure 5 shows the comparison between the experiments and simulations for the conglomerate gravel–steel interface experiments. It is evident that overall, all the models are capable of adequately reproducing the SSI behaviors. The simulations of shear stress and normal displacement, under different, show a high degree of agreement with the experimental data for all models. Additionally, all models successfully replicate the general pattern of the normal displacement. The experimental findings indicate that the shear stress amplitude remains relatively constant as the number of cycles increases. One possible explanation for this is that the amplitude of the shear displacement is large enough for the interface to reach the critical state. Consequently, particle breakage does not have a significant impact on the shear stress because of the unique nature of the critical state.

However, this phenomenon does not hold true for the normal displacement. Research studies [13, 50, 51] have shown significant

10969853, 2024, 17, Downloaded from https://onlinelibrary.wiley.com/doi/10.1002/nag.3831 by HONG KONG POLYTECHNIC UNIVERSITY HU NG HOM, Wiley Online Library on [26/11/2024]. See the Terms and Conditions (https://onlinelibrary.wiley.com/terms-and-conditions) on Wiley Online Library for rules of use; OA articles are governed by the applicable Creative Commons License

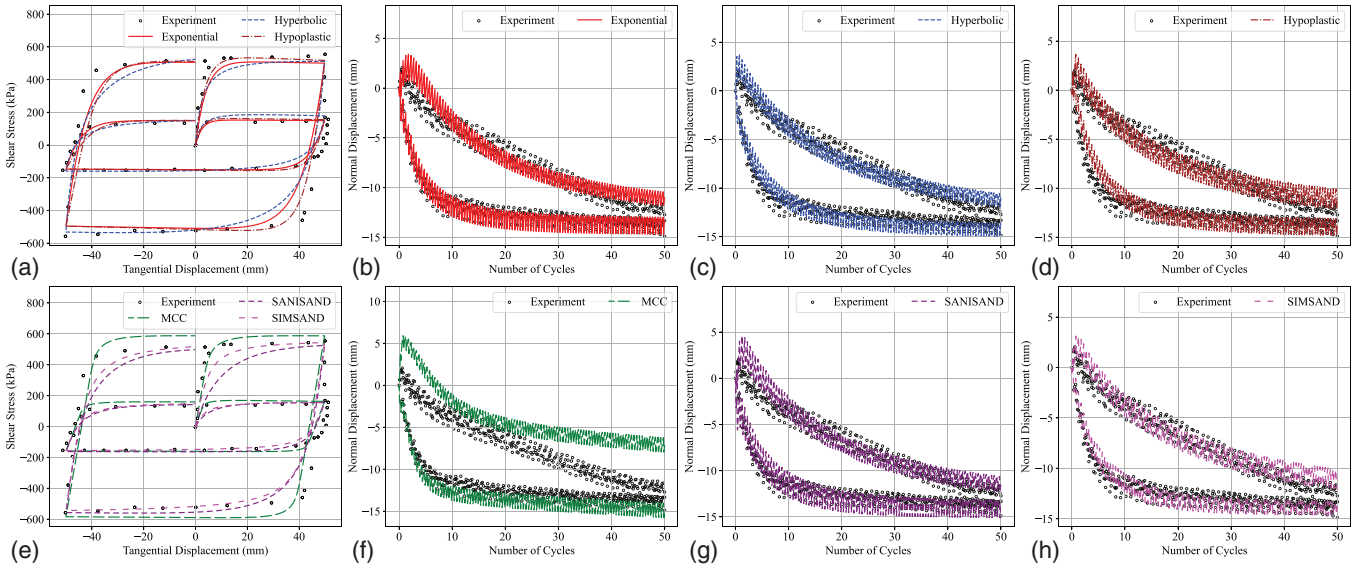

FIGURE 5 | Comparison between the experiments and simulations for the conglomerate gravel–steel interface experiments: (a) shear stress for nonlinear incremental models; (b)–(d) normal displacement for exponential model, hyperbolic model, and hypoplastic model; (e) shear stress for elastoplastic models; (f)–(h) normal displacement for MCC model, SANISAND model, and SIMSAND model.

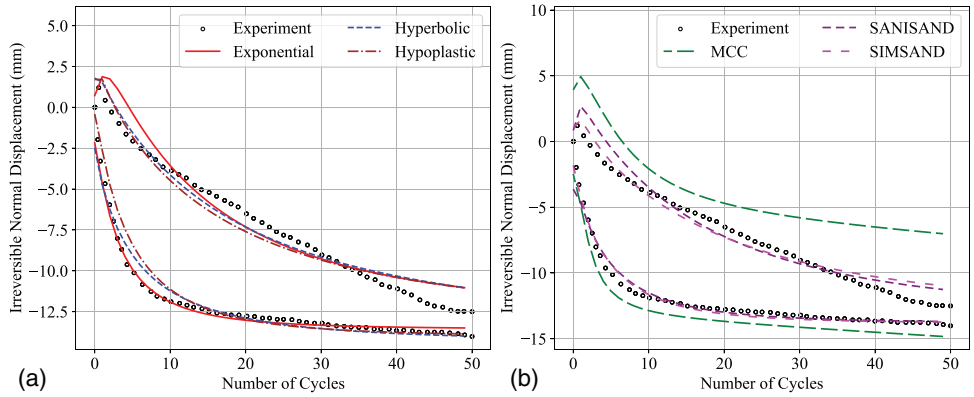

FIGURE 6 | Comparison between the experiments and simulations for the irreversible normal displacement conglomerate gravel–steel interface experiments: (a) nonlinear incremental models; (b) elastoplastic models.

normal displacement accumulation under cyclic loading, which is primarily attributed to particle breakage. Fine particles that are crushed during shearing can easily fill the voids within the soil layers, leading to a continuous development of the normal displacement.

To simulate continuous normal displacement under cyclic loading, the critical state theory used in the models incorporates plastic work-based particle breakage formulation that has been previously used in studies [13, 15], as shown in Equations (16) and (17). The comparison between simulations and experiments of irreversible normal displacement, which is the average normal displacement in each cycle using different models, is shown in Figure 6. It is apparent that all models, except for the MCC model, can simulate the development of irreversible normal displacement, while the impact of normal stress on residual irreversible normal displacement appears to be insignificant, verifying the results reported by Zhang et al. [8].

To explain this phenomenon, the evolution of the normal displacement for different models is shown below:

$$\mathrm{d}\varepsilon_n = \frac{K_n^*}{K_n^* + K'} \mathrm{d}\gamma^* \begin{cases} A_d^*(\tan\phi_{pt} - \eta) & \text{Except MCC/SANISAND} \\ A_d^*(\alpha^d - \alpha) & \text{SANISAND} \\ \dfrac{(\tan\phi_c)^{n+1} - \eta^{n+1}}{(n+1)/n \cdot \eta^n} & \text{MCC} \end{cases} \tag{45}$$

where $K_n^* = K_n'$ and $A_d^* = A_d'$ for the hypoplastic model and $K_n^* = K_n$ and $A_d^* = A_d$ for other models, $\mathrm{d}\gamma^* = \mathrm{d}\gamma$ for nonlinear incremental models, and $\mathrm{d}\gamma^* = \mathrm{d}\gamma^p$ for elastoplastic models. It can be seen from the above equations that the normal behavior is controlled by both the interface's normal boundary condition (represented by the stiffness K') and the soil's normal behavior (represented by the soil's normal stiffness K_n and the dilatancy behavior). When the normal boundary of the interface is not

10969853, 2024, 17, Downloaded from https://onlinelibrary.wiley.com/doi/10.1002/nag.3831 by HONG KONG POLYTECHNIC UNIVERSITY HU NG HOM, Wiley Online Library on [26/11/2024]. See the Terms and Conditions (https://onlinelibrary.wiley.com/terms-and-conditions) on Wiley Online Library for rules of use; OA articles are governed by the applicable Creative Commons License

constrained ($K' = 0$), the above equations degenerate into stress–dilatancy equations similar to the general soil models. Since the SANISAND model uses the same equation for the slope of the dilatancy surface α^d as $\tan\phi_{pt}$ and the rotation index α is very close to the stress ratio η, Equation (23) can be generalized as

$$d\varepsilon_n \simeq \frac{K_n^*}{K_n^* + K'} d\gamma^* \begin{cases} A_d^*(\tan\phi_{pt} - \eta) & \text{Except MCC} \\ \dfrac{(\tan\phi_c)^{n+1} - \eta^{n+1}}{(n+1)/n \cdot \eta^n} & \text{MCC} \end{cases} \tag{46}$$

For all models except for the MCC model, the phase transformation stress ratio $\tan\phi_{pt}$ is a function of the current density state and the critical state

$$\tan\phi_{pt} = \left(\frac{e}{e_c}\right)^{n_d} \tan\phi_c \tag{47}$$

where $\tan\phi_c$ is the slope of the CSL. The above equation for the dynamic phase transformation stress ratio $\tan\phi_{pt}$, implies that in loose sand conditions with $e > e_c$, $\tan\phi_{pt}$ is greater than $\tan\phi_c$, which leads to persistent shear contraction behaviors; in dense sand conditions with $e < e_c$, $\tan\phi_{pt}$ is less than $\tan\phi_c$, which allows the dense sand to be contracted and then dilated.

To roughly estimate the generated normal displacement during cyclic loading, we assume that the interface is sheared with the path $0 \to u_0 \to 0 \to -u_0 \to 0$ controlled by the tangential displacement under CNL condition. To obtain an analytical solution for the total normal displacement within a single cycle, we assume that (1) the critical state is reached at the end of every reversal points, thus the mean shear stress ratio is approximately equal to half of its critical value $\tan\phi_c$; (2) the void ratio and critical void ratio remain constant within a single step, comparing to the long-term effect of particle breakage. Then the accumulated normal displacement can be roughly calculated as

$$\begin{cases} d\varepsilon_{n_1} = \sum_{i=1}^{n} A_d \left[\left(\dfrac{e_0 - (1+e_0)\sum_{j=1}^{i-1} d\varepsilon_{n_j}}{e_c - \sum_{j=1}^{i-1} \Delta e_{c_j}} \right)^{n_d} \tan\phi_c - \eta_i \right] \dfrac{d\gamma}{n} \\ \quad \approx A_d \left[\left(\dfrac{e_0}{e_c} \right)^{n_d} \tan\phi_c - \bar{\eta} \right] d\gamma \\ d\varepsilon_{n_2} \approx A_d \left[\left(\dfrac{e_1}{e_c} \right)^{n_d} \tan\phi_c + \bar{\eta} \right] d\gamma, \quad e_1 = e_0 - (1+e_0) d\varepsilon_{n_2} \\ d\varepsilon_{n_3} \approx A_d \left[\left(\dfrac{e_2}{e_c} \right)^{n_d} \tan\phi_c + \bar{\eta} \right] d\gamma, \quad e_2 = e_1 - (1+e_0) d\varepsilon_{n_3} \\ d\varepsilon_{n_4} \approx A_d \left[\left(\dfrac{e_3}{e_c} \right)^{n_d} \tan\phi_c - \bar{\eta} \right] d\gamma, \quad e_3 = e_2 - (1+e_0) d\varepsilon_{n_4} \end{cases} \tag{48}$$

The accumulated normal displacement can be calculated as

$$\begin{aligned} d\varepsilon_n &= \sum_{i=1}^{4} d\varepsilon_{n_i} = A_d \tan\phi_c \left[(X-3Y)^{n_d} - (X-2Y)^{n_d} \right. \\ &\quad \left. - (X-Y)^{n_d} + X^{n_d} \right] d\gamma X = \frac{e_0}{e_c}, \\ Y &= \frac{(1+e_0) A_d \tan\phi_c}{e_c} X^{n_d} \end{aligned} \tag{49}$$

when $n_d = 0$, the stress–dilatancy relationship degrades to the classical Rowe's dilatancy equation, and the accumulated normal displacement $d\varepsilon_n$ degrades to 0. Although this may not hold true within the first few circles, where the stress–dilatancy relationship is highly nonlinear, and consequently, the error generated by the one-step simulation cannot be ignored. This proves that the classical critical state theory cannot reflect the accumulated normal displacement under cyclic loading, as reported in previous studies [13, 15]. For the case of $n_d = 1$, the accumulated normal displacement $d\varepsilon_n$ also degrades to 0 if we consider the critical void ratio e_c as a constant. However, with the consideration of the particle breakage, e_c decreases during the shearing, the accumulated normal displacement can be calculated by

$$\begin{aligned} d\varepsilon_n &= A_d \tan\phi_c [(X_1 - X_2 - X_3 + X_4) + (Y_2 + 2Y_3 - 3Y_4)] \\ d\gamma &= A_d \tan\phi_c e_0 [(1-h)F + hG] d\gamma \end{aligned} \tag{50}$$

$$F = \frac{1}{e_{c_1}} - \frac{1}{e_{c_2}} - \frac{1}{e_{c_3}} + \frac{1}{e_{c_4}} \tag{51}$$

$$G = \frac{1}{e_{c_2}} + \frac{1}{e_{c_3}} - \frac{2}{e_{c_4}} \tag{52}$$

$$h = \frac{A_d(1+e_0)}{e_{c_1}} \tag{53}$$

It is noteworthy that the accumulated normal displacement in a single cycle can be divided into two components denoted as F and G. Considering the long-term effect of particle breakage, it is reasonable to assume a gradual linear decline in the critical state void ratio throughout a single cycle, that is, $e_{c_2} = e_{c_1} - \Delta e_c$, $e_{c_3} = e_{c_1} - 2\Delta e_c$, and $e_{c_4} = e_{c_1} - 3\Delta e_c$. Then, F and G can be calculated as

$$F = \frac{2\Delta e_{c_1}^2 (2e_{c_1} - 3\Delta e_c)}{e_{c_1}(e_{c_1} - \Delta e_c)(e_{c_1} - 2\Delta e_c)(e_{c_1} - 3\Delta e_c)} \approx \frac{4\Delta e_c^2}{e_{c_1}^3} \approx 0 \tag{54}$$

$$G = -\frac{\Delta e_c (3e_{c_1} - 5\Delta e_c)}{(e_{c_1} - \Delta e_c)(e_{c_1} - 2\Delta e_c)(e_{c_1} - 3\Delta e_c)} \approx -\frac{3\Delta e_c}{e_{c_1}^2} < 0 \tag{55}$$

given that Δe_c is a very small value, F represents the second-order term with respect to Δe_c, whereas G represents the first-order term. Consequently, F is negligible in comparison to G. Thus, F approaches 0, whereas G exhibits a negative value. Hence, a logical inference can be made that F signifies reversible normal displacement, and G denotes irreversible normal displacement, which has been recognized in previous study [8]. Notably, this implication is interesting since it implies that incorporating particle breakage enables the modeling of both reversible and irreversible normal displacement during cyclic loading without explicit consideration of the stress–dilatancy relationship.

Zhang et al. [8] pointed out that the irreversible normal displacement monotonically increases with the number of cycles and finally reaches a stable value that is not dependent on the stress level but is related to the soil properties. They used a hyperbolic function to describe the relationship between the irreversible normal displacement and the number of cycles. To verify this, the evolution of the critical void ratio during cyclic loading described in Equations (16) and (17) is shown in Figure 7. The e_{c0} and e_{cu}

10969853, 2024, 17, Downloaded from https://onlinelibrary.wiley.com/doi/10.1002/nag.3831 by HONG KONG POLYTECHNIC UNIVERSITY HU NG HOM, Wiley Online Library on [26/11/2024]. See the Terms and Conditions (https://onlinelibrary.wiley.com/terms-and-conditions) on Wiley Online Library for rules of use; OA articles are governed by the applicable Creative Commons License

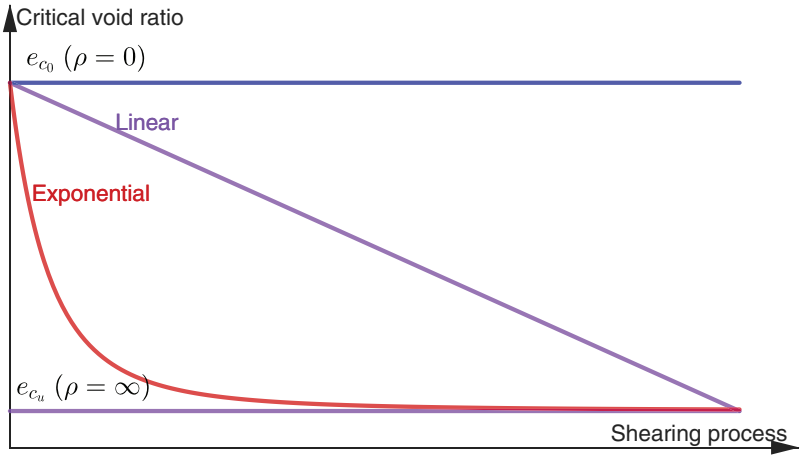

FIGURE 7 | Evolution of the critical void ratio during cyclic loading.

lines show the cases where the parameter ρ is 0 and ∞, and the linear line shows the linear decline of the critical void ratio during the shearing to simplify the calculation and demonstrate the relationship between particle breakage and the accumulated normal displacement. According to the above equations, the accumulated irreversible normal displacement can be calculated by

$$\varepsilon_n = A_d \tan\phi_c e_0 \mathrm{d}\gamma \sum_{i=0}^{n} h_i G_i = -3A_d \tan\phi_c e_0 A_d (1+e_0)\mathrm{d}\gamma \sum_{i=0}^{n} \frac{\Delta e_{c_i}}{e_{c_i}^3}$$

$$= -C \sum_{i=0}^{n} \frac{\Delta e_{c_i}}{e_{c_i}^3} \text{ with } C = 3A_d \tan\phi_c e_0 A_d (1+e_0)\mathrm{d}\gamma \quad (56)$$

For the cases of $\rho = 0$ (no particle breakage, $e_{c_0} = e_{c_u}$), the accumulated irreversible normal displacement can be calculated by

$$\varepsilon_n = -C \sum_{i=0}^{n} \frac{\Delta e_{c_i}}{e_{c_i}^3} = -\frac{e_{c_0} - e_{cu}}{e_{c_0}^3} C = -\frac{e_{c_u}}{e_{c_0}^2}\left(\frac{1}{e_{c_u}} - \frac{1}{e_{c_0}}\right) C = 0 \quad (57)$$

For the cases of $\rho = \infty$ (the particle breakage is developed very fast), the accumulated irreversible normal displacement can be calculated by

$$\varepsilon_n = -C \sum_{i=0}^{n} \frac{\Delta e_{c_i}}{e_{c_i}^3} = -\frac{e_{c_0} - e_{cu}}{e_{c_u}^3} C = -\frac{e_{c_0}}{e_{c_u}^2}\left(\frac{1}{e_{c_u}} - \frac{1}{e_{c_0}}\right) C \quad (58)$$

The complex nature of the exponential decrease in critical void ratio makes it impossible to obtain an analytical solution for the accumulated irreversible normal displacement. Thus, a linear approximation of the critical void ratio decline is used to simplify the calculation. In this case, the accumulated irreversible normal displacement can be calculated by

$$\varepsilon_n = -C \lim_{n\to\infty} \sum_{i=0}^{n} \frac{\Delta e_{c_i}}{e_{c_i}^3} = -C \lim_{n\to\infty} \sum_{i=0}^{n} \frac{(e_{c_0} - e_{cu})/n}{\left[e_{c_0} - i/n(e_{c_0} - e_{cu})\right]^3}$$

$$= -C \lim_{n\to\infty} \frac{n^2}{2(e_{c_0} - e_{c_u})^2}\left[\Psi''\left(\frac{n e_{c_u}}{e_{c_0} - e_{c_u}}\right) - \Psi''\left(1 + \frac{n e_{c_0}}{e_{c_0} - e_{c_u}}\right)\right]$$

$$= -\frac{1}{2}\left(\frac{1}{e_{c_u}^2} - \frac{1}{e_{c_0}^2}\right) C = -\frac{(e_{c_0} + e_{c_u})/2}{e_{c_0} e_{c_u}}\left(\frac{1}{e_{c_u}} - \frac{1}{e_{c_0}}\right) C \quad (59)$$

where $\Psi''(\cdot)$ is the second-order polygamma function. It is well known that the occurrence of particle breakage depends on the stress level, which in turn governs the duration of the shearing process involving the rearrangement of the particles. Consequently, the nonlinearity of the critical void ratio's reduction is solely influenced by the nonlinear nature of the breakage phenomena. Thus, combined with the equations provided earlier, it can be concluded that the irreversible normal displacement is independent of the stress level but influenced by the initial and final states of the soil properties such as initial density (e_0), CSL slope ($\tan\phi_c$), dilatancy (A_d), and initial/ultimate critical void ratio (e_{c0} and e_{cu}) associated with particle breakage. This provides a theoretical foundation for statements made by Zhang et al. [8]. Considering the nonlinear impact of particle breakage on critical void ratio, it follows that the accumulated irreversible normal displacement should also exhibit nonlinear behavior with respect to the particle breakage parameters ρ and n_w.

The analysis above demonstrates that the introduction of particle breakage allows all models, except for the MCC model, to successfully simulate irreversible normal displacement. The MCC model cannot simulate irreversible normal displacement, as it does not incorporate the particle breakage effect. However, by introducing the stress–dilatancy relationship described in Equation (45), it can partially simulate irreversible normal displacement. Nevertheless, due to the strong stress dependency of the stress–dilatancy relationship, the simulation of irreversible normal displacement can only be achieved at specific stress levels. This suggests that the successful simulation of irreversible normal displacement is merely a result of curve-fitting and does not capture the actual underlying mechanism of the irreversible normal displacement.

To further demonstrate the effect of the particle breakage on the irreversible normal displacement, the models are calibrated without considering the breakage effect. Table 6 shows the identified model parameters for the conglomerate gravel–steel experiments without considering the breakage effect. It can be seen that the calibrated fitness of the models is higher when the breakage effect is not considered, suggesting the significance of the breakage effect for the simulation of irreversible

10969853, 2024, 17, Downloaded from https://onlinelibrary.wiley.com/doi/10.1002/nag.3831 by HONG KONG POLYTECHNIC UNIVERSITY HU NG HOM, Wiley Online Library on [26/11/2024]. See the Terms and Conditions (https://onlinelibrary.wiley.com/terms-and-conditions) on Wiley Online Library for rules of use; OA articles are governed by the applicable Creative Commons License

TABLE 6 | Identified model parameters for the conglomerate gravel–steel experiments without considering the breakage effect.

Models	R_d	ϕ	G_0	A_d	R	λ	ξ	e_{ref0}	n_p	n_d	v_i	h_0	k_p	RMSE
Exponential	6.1	34.3	602	0.38	3.60	0.03	0.10	2.00	0.03	0.01				14.1%
Hyperbolic	7.3	40.3	1167	0.24	8.66	0.05	0.03	2.00	0.00	0.12				15.4%
Hypoplastic	8.1	34.4	2759			0.09	0.01	1.94	19.17	0.02	0.37			14.7%
SANISAND	11.6	36.7	753	1.99	0.26	0.46	0.00	0.85	0.00	0.04		0.39		15.6%
SIMSAND	35.2	41.1	3082	0.28	9.99	1.09	0.01	1.38	1.66	0.00			0.01	15.8%

Abbreviation: RMSE, root mean square error.

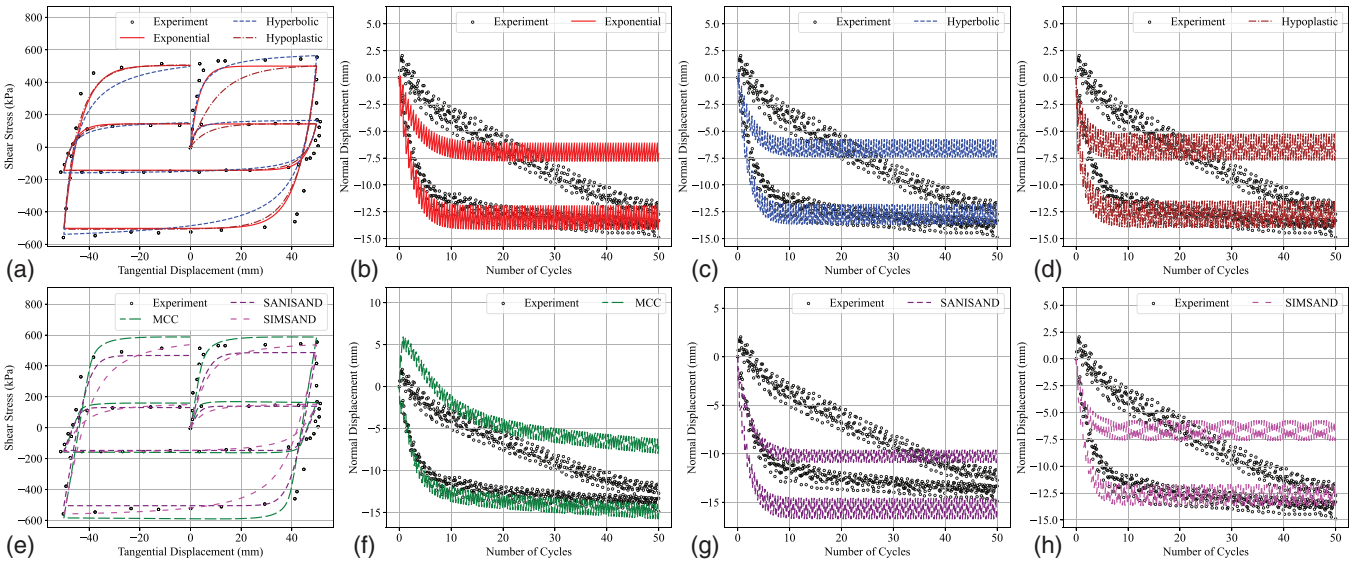

FIGURE 8 | Comparison between the experiments and simulations for the conglomerate gravel–steel interface experiments without considering the breakage effect: (a) shear stress for nonlinear incremental models; (b)–(d) normal displacement for exponential model, hyperbolic model, and hypoplastic model; (e) shear stress for elastoplastic models; (f)–(h) normal displacement for MCC model, SANISAND model, and SIMSAND model.

normal displacement. The comparison between the experiments and simulations for the conglomerate gravel–steel experiments without considering the breakage effect is shown in Figure 8. The results indicate that when the breakage effect is not taken into account, the models fail to replicate the irreversible normal displacement observed in experiments, similar to the MCC model that does not incorporate the breakage effect. The irreversible normal displacement exhibits high sensitivity to stress levels, contrary to experimental findings where it stabilizes regardless of stress levels. This further demonstrates the significance of the breakage effect for the simulation of irreversible normal displacement.

3.3.3 | Crushed Quartz–Steel Experiments: Stress Degradation Under CNS Condition

The crushed quartz–steel experiments are performed using simple shear tests by Fakharian [48]. One constant normal load experiment with the initial normal stress of 100 kPa and one constant normal stiffness experiment with the initial normal stress of 300 kPa and the normal stiffness of 400 kN/mm are conducted.

Figure 9 shows the comparison between the experiments and simulations for the crushed quartz–steel experiments under constant normal load and constant normal stiffness. The results show that the simulations are highly in agreement with the experiments for all models. Unlike the gravel–steel experiments, the shear stress amplitude decreases along with the number of cycles because of the particle breakage when a great number of cycles are applied. The particle breakage only takes effect with a large number of cycles since it relates to the accumulated plastic work induced by the shearing process. The model parameters identified from the experiments shown in Table 5 also show that the breakage effect-related parameter ρ is significant for the crushed quartz–steel experiments.

The degradation of the normal stress under CNS condition is shown in Figure 10, where the degradation factor is defined as the ultimate shear stress in each cycle divided by the ultimate shear stress in the first cycle [52]. All models effectively simulate the stress degradation observed in the CNS experiments. Nevertheless, the degradation curve in the hypoplastic model exhibits an unconventional pattern, likely due to the significant nonlinearity of the model and the limited availability of cyclic data, as data only from three specific cycles are utilized.

10969853, 2024, 17, Downloaded from https://onlinelibrary.wiley.com/doi/10.1002/nag.3831 by HONG KONG POLYTECHNIC UNIVERSITY HU NG HOM, Wiley Online Library on [26/11/2024]. See the Terms and Conditions (https://onlinelibrary.wiley.com/terms-and-conditions) on Wiley Online Library for rules of use; OA articles are governed by the applicable Creative Commons License

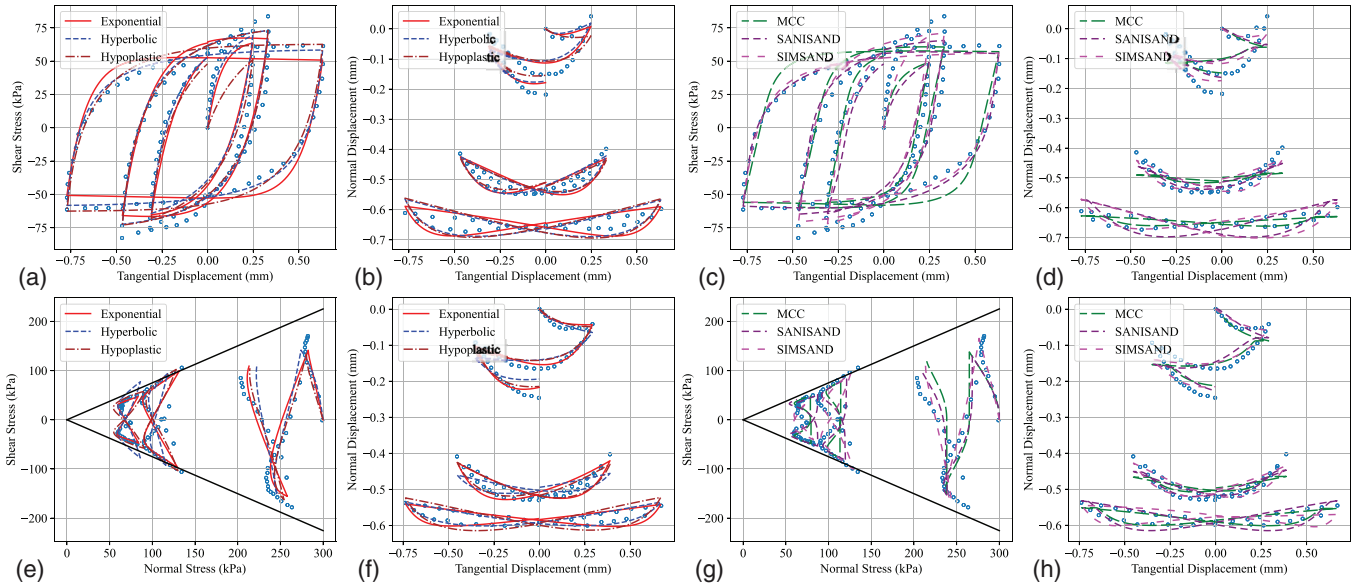

FIGURE 9 | Comparison between the experiment and simulation for the crushed quartz–steel experiments: (a)–(d) shear stress vs. tangential displacement and normal displacement vs. tangential displacement for nonlinear incremental models and elastoplastic models with constant normal stress of 100 kPa; (e)–(h) shear stress vs. normal stress and normal displacement vs. tangential displacement for nonlinear incremental models and elastoplastic models with constant normal stiffness of 400 kN/mm and initial normal stress of 300 kPa.

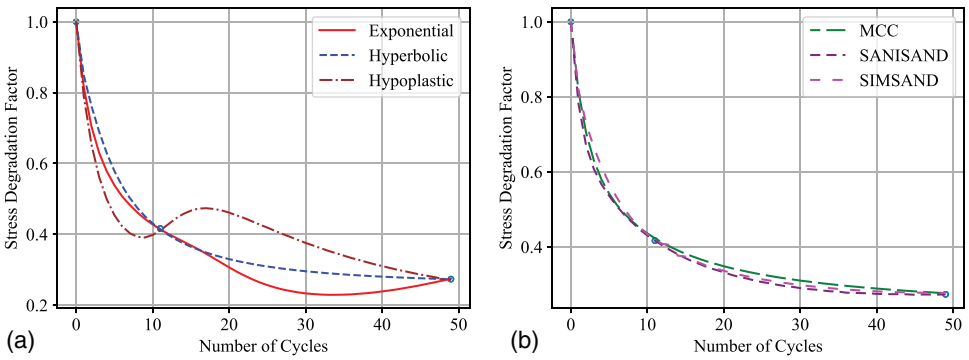

FIGURE 10 | Comparison between the experiment and simulation for stress degradation of the crushed quartz–steel experiments: (a) nonlinear incremental models; (b) elastoplastic models.

To explain this phenomenon, the evolution of the normal stress for different models is shown below

$$\mathrm{d}\sigma_n = -K'\mathrm{d}\varepsilon_n \simeq \frac{K_n^* K'}{K_n^* + K'}\mathrm{d}\gamma \begin{cases} A_d^*(\tan\phi_{pt} - \eta) & \text{Except MCC} \\ \dfrac{\tan\phi_c^{n+1} - \eta^{n+1}}{(n+1)/n \cdot \eta^n} & \text{MCC} \end{cases} \tag{60}$$

Since the normal stress increment is linear with the normal displacement increment, the evolution of the normal stress is very much like the irreversible normal displacement, as shown in Figure 6. Under constant normal stiffness, the accumulated normal displacement is generated due to particle breakage, resulting in the degradation of the normal stress, and consequently the degradation of the shear stress. Equation (60) illustrates that the rate of stress degradation is influenced by the normal boundary condition of the interface, denoted as stiffness K'. When the normal load is held constant ($K' = 0$), the stress degradation disappears. In contrast, under the condition of constant volume ($K' = \infty$), the stress degradation is maximized, aligning with experimental observations [7].

4 | Conclusions

In this paper, six different SSI models considering the cyclic loading effect are proposed or adopted, including three nonlinear incremental models (exponential, hyperbolic, and hypoplastic) and three elastoplastic models (MCC, SANISAND, and SIMSAND). To incorporate the cyclic loading effect, several different approaches are presented, including the stress reversal method used in exponential, hyperbolic, and SIMSAND models, bounding surface theory, and the hypoplastic modeling method. For a fair comparison, all SSI models are calibrated against interface experiments under various conditions based on the optimization method. The simulation results show that all the models are able to reproduce the SSI behaviors with satisfaction under different stress levels and boundary conditions.

10969853, 2024, 17, Downloaded from https://onlinelibrary.wiley.com/doi/10.1002/nag.3831 by HONG KONG POLYTECHNIC UNIVERSITY HU NG HOM, Wiley Online Library on [26/11/2024]. See the Terms and Conditions (https://onlinelibrary.wiley.com/terms-and-conditions) on Wiley Online Library for rules of use; OA articles are governed by the applicable Creative Commons License

Evaluation of the model's performance in simulating the effects of shearing amplitude, accumulated normal displacement, and stress degradation under cyclic loading is undertaken. The findings indicate that all models successfully replicate cyclic experiments across various shearing amplitudes. Notably, incorporating particle breakage enables the modeling of both reversible and irreversible normal displacement during cyclic loading in all models, except for the MCC model. The irreversible normal displacement generated by the particle breakage depends significantly on soil properties such as initial density, CSL slope, dilatancy parameter, and particle breakage parameters.

The MCC model demonstrates limited capability in simulating irreversible normal displacement, attributed to the robust stress dependency of the stress–dilatancy relationship. Furthermore, all models can replicate the degradation of normal stress under constant normal stiffness, attributed to the accumulation of normal displacement resulting from particle breakage. Overall, all models are capable of simulating the SSI behaviors under cyclic loading, providing a comprehensive understanding of the SSI response under cyclic loading.

Acknowledgments

The financial support is provided by the projects (Grants 15217220 and N_PolyU534/20) from the Research Grants Council (RGC) of Hong Kong and Research Centre for Resources Engineering towards Carbon Neutrality (RCRE) of The Hong Kong Polytechnic University (Grants 1-BBEM).

Data Availability Statement

All data that support the findings of this study are available from the corresponding author upon reasonable request.

References

1. M. Uesugi and H. Kishida, "Influential Factors of Friction Between Steel and Dry Sands," *Soils and Foundations* 26, no. (2) (1986): 33–46, https://doi.org/10.3208/sandf1972.26.2_33.

2. K. Fakharian and E. Evgin, "Cyclic Simple-Shear Behavior of Sand-Steel Interfaces Under Constant Normal Stiffness Condition," *Journal of Geotechnical and Geoenvironmental Engineering* 123, no. 12 (1997): 1096–1105, https://doi.org/10.1061/(Asce)1090-0241(1997)123:12(1096).

3. J. D. Frost, J. T. DeJong, and M. Recalde, "Shear Failure Behavior of Granular-Continuum Interfaces," *Engineering Fracture Mechanics* 69, no. 17 (2002): 2029–2048, https://doi.org/10.1016/S0013-7944(02)00075-9.

4. J. T. DeJong, M. F. Randolph, and D. J. White, "Interface Load Transfer Degradation During Cyclic Loading: A Microscale Investigation," *Soils and Foundations* 43, no. 4 (2003): 81–93, https://doi.org/10.3208/sandf.43.4_81.

5. C. S. Desai, S. K. Pradhan, and D. Cohen, "Cyclic Testing and Constitutive Modeling of Saturated Sand–Concrete Interfaces Using the Disturbed State Concept," *International Journal of Geomechanics* 5, no. 4 (2005): 286–294.

6. T. A. Oumarou and E. Evgin, "Behaviour of a Sand-Steel Plate Interface," *Canadian Geotechnical Journal* 42(6): 1695–1704, https://doi.org/10.1139/t05-083.

7. G. Mortara, A. Mangiola, and V. N. Ghionna, "Cyclic Shear Stress Degradation and Post-Cyclic Behaviour From Sand-Steel Interface Direct Shear Tests," *Canadian Geotechnical Journal* 44, no. 7 (2007): 739–752, https://doi.org/10.1139/T07-019.

8. G. Zhang, L. Wang, and J. M. Zhang, "Dilatancy of the Interface Between a Structure and Gravelly Soil," *Géotechnique* 61, no. 1 (2011): 75–84, https://doi.org/10.1680/geot.9.P.051.

9. S. Pra-ai and M. Boulon, "Soil-Structure Cyclic Direct Shear Tests: A New Interpretation of the Direct Shear Experiment and Its Application to a Series of Cyclic Tests," *Acta Geotechnica* 12, no. 1 (2017): 107–127, https://doi.org/10.1007/s11440-016-0456-6.

10. D. Feng, J. Zhang, and W. Hou, "Role of Normal Stiffness in 3D Cyclic Behavior of Gravel–Steel Interface From Large-Scale Direct Shear Tests," *Acta Geotechnica* 16, no. 1 (2021): 151–165, https://doi.org/10.1007/s11440-020-01006-7.

11. G. Zhang and J. M. Zhang, "Unified Modeling of Monotonic and Cyclic Behavior of Interface Between Structure and Gravelly Soil," *Soils and Foundations* 48, no. 2 (2008): 231–245, https://doi.org/10.3208/sandf.48.231.

12. I. Shahrour and F. Rezaie, "An Elastoplastic Constitutive Relation for the Soil-Structure Interface Under Cyclic Loading," *Computers and Geotechnics* 21, no. 1 (1997): 21–39, https://doi.org/10.1016/S0266-352x(97)00001-3.

13. J. M. Liu, D. G. Zou, and X. J. Kong, "A Three-Dimensional State-Dependent Model of Soil-Structure Interface for Monotonic and Cyclic Loadings," *Computers and Geotechnics* 61 (2014): 166–177, https://doi.org/10.1016/j.compgeo.2014.05.012.

14. H. Stutz, "Hypoplastic Models for Soil-Structure Interfaces: Modelling and Implementation" (PhD thesis, Kiel University, 2016).

15. J. Yang and Z. Y. Yin, "Soil-Structure Interface Modeling With the Nonlinear Incremental Approach," *International Journal for Numerical and Analytical Methods in Geomechanics* 45, no. 10 (2021): 1381–1404, https://doi.org/10.1002/nag.3206.

16. C. S. Desai, E. C. Drumm, and M. M. Zaman, "Cyclic Testing and Modeling of Interfaces," *Journal of Geotechnical Engineering-Asce* 111, no. 6 (1985): 793–815, https://doi.org/10.1061/(Asce)0733-9410(1985)111:6(793).

17. H. L. Wang, Z. Y. Yin, Y. F. Jin, and X. Q. Gu, "Evaluation of Soil–Structure Interface Models," *Journal of Geotechnical and Geoenvironmental Engineering* 150, no. 7 (2024): 04024050, https://doi.org/10.1061/JGGEFK.GTENG-11486.

18. M. Arnold and I. Herle, "Hypoplastic Description of the Frictional Behaviour of Contacts," in *Proceedings of the 6th European Conference on Numerical Methods in Geotechnical Engineering*, (London, CRC Press, 2006), 101–106, https://doi.org/10.1201/9781439833766.

19. H. L. Wang, Y. F. Jin, Z. Y. Yin, and X. Q. Gu, "Uncertainty Quantification of Soil–Structure Interface Properties With an Enhanced Hypoplastic Interface Model," *International Journal of Geomechanics* 24, no. 6 (2024): 04024103, https://doi.org/10.1061/IJGNAI.GMENG-9248.

20. N. Navayogarajah, C. S. Desai, and P. D. Kiousis, "Hierarchical Single–Surface Model for Static and Cyclic Behavior of Interfaces," *Journal of Engineering Mechanics* 118, no. 5 (1992): 990–1011, https://doi.org/10.1061/(asce)0733-9399(1992)118:5(990).

21. G. Mortara, M. Boulon, and V. N. Ghionna, "A 2-D Constitutive Model for Cyclic Interface Behaviour," *International Journal for Numerical and Analytical Methods in Geomechanics* 26, no. 11 (2002): 1071–1096, https://doi.org/10.1002/nag.236.

22. H. Liu and H. I. Ling, "Constitutive Description of Interface Behavior Including Cyclic Loading and Particle Breakage Within the Framework of Critical State Soil Mechanics," *International Journal for Numerical and Analytical Methods in Geomechanics* 32, no. 12 (2008): 1495–1514, https://doi.org/10.1002/nag.682.

23. A. Lashkari, "Modeling of Sand-Structure Interfaces Under Rotational Shear," *Mechanics Research Communications* 37, no. 1 (2010): 32–37, https://doi.org/10.1016/j.mechrescom.2009.09.005.

24. S. C. D'Aguiar, A. Modaressi-Farahmand-Razavi, J. A. dos Santos, and F. Lopez-Caballero, "Elastoplastic Constitutive Modelling of Soil-Structure Interfaces Under Monotonic and Cyclic Loading," *Computers*

10969853, 2024, 17, Downloaded from https://onlinelibrary.wiley.com/doi/10.1002/nag.3831 by HONG KONG POLYTECHNIC UNIVERSITY HU NG HOM, Wiley Online Library on [26/11/2024]. See the Terms and Conditions (https://onlinelibrary.wiley.com/terms-and-conditions) on Wiley Online Library for rules of use; OA articles are governed by the applicable Creative Commons License

and Geotechnics 38, no. 4 (2011): 430–447, https://doi.org/10.1016/j.compgeo.2011.02.006.

25. S. Burlon, H. Mroueh, and J. P. Cao, "'Skipped Cycles' Method for Studying Cyclic Loading and Soil–Structure Interface," *Computers and Geotechnics* 61 (2014): 209–220, https://doi.org/10.1016/j.compgeo.2014.05.007.

26. J. Duriez and E. Vincens, "Constitutive Modelling of Cohesionless Soils and Interfaces With Various Internal States: An Elasto-Plastic Approach," *Computers and Geotechnics* 63 (2015): 33–45, https://doi.org/10.1016/j.compgeo.2014.08.001.

27. M. Saberi, C. D. Annan, and J. M. Konrad, "Constitutive Modeling of Gravelly Soil-Structure Interface Considering Particle Breakage," *Journal of Engineering Mechanics* 143, no. 8 (2017): 04017044, https://doi.org/10.1061/(Asce)Em.1943-7889.0001246.

28. M. Saberi, C. D. Annan, and J. M. Konrad, "Three-Dimensional Constitutive Model for Cyclic Behavior of Soil-Structure Interfaces," *Soil Dynamics and Earthquake Engineering* 134 (2020): 106162, https://doi.org/10.1016/j.soildyn.2020.106162.

29. P. Staubach, J. Machaček, and T. Wichtmann, "Novel Approach to Apply Existing Constitutive Soil Models to the Modelling of Interfaces," *International Journal for Numerical and Analytical Methods in Geomechanics* 46, no. 7 (2022): 1241–1271, https://doi.org/10.1002/nag.3344.

30. G. W. Clough and J. M. Duncan, "Finite Element Analyses of Retaining Wall Behavior," *Journal of the Soil Mechanics and Foundations Division* 97, no. 12 (1971): 1657–1673, https://doi.org/10.1061/JSFEAQ.0001713.

31. S. Wang, W. Wu, Z. Y. Yin, C. Peng, and X. He, "Modelling the Time-Dependent Behaviour of Granular Material With Hypoplasticity," *International Journal for Numerical and Analytical Methods in Geomechanics* 42, no. 12 (2018): 1331–1345, https://doi.org/10.1002/nag.2793.

32. J. Yang and Z. Y. Yin, "Unified Modeling of Interface Between Structured Clay or Crushable Sand and Structure," *Journal of Engineering Mechanics* 149, no. 8 (2023): 04023052, https://doi.org/10.1061/JENMDT.EMENG-6997.

33. M. Taiebat and Y. F. Dafalias, "SANISAND: Simple Anisotropic Sand Plasticity Model," *International Journal for Numerical and Analytical Methods in Geomechanics* 32, no. 8 (2008): 915–948, https://doi.org/10.1002/nag.651.

34. Z. Y. Yin, H. W. Huang, and P. Y. Hicher, "Elastoplastic Modeling of Sand–Silt Mixtures," *Soils and Foundations* 56, no. 3 (2016): 520–532, https://doi.org/10.1016/j.sandf.2016.04.017.

35. L. Hu and J. Pu, "Testing and Modeling of Soil-Structure Interface," *Journal of Geotechnical and Geoenvironmental Engineering* 130, no. 8 (2004): 851–860, https://doi.org/10.1061/(ASCE)1090-0241(2004)130:8(851).

36. R. D. Tovar-Valencia, A. Galvis-Castro, R. Salgado, and M. Prezzi, "Effect of Surface Roughness on the Shaft Resistance of Displacement Model Piles in Sand," *Journal of Geotechnical and Geoenvironmental Engineering* 144, no. 3 (2018): 04017120, https://doi.org/10.1061/(ASCE)GT.1943-5606.0001828.

37. E. Wernick, "Skin Friction of Cylindrical Anchors in Non-Cohesive Soils," *Symposium on Soil Reinforcing and Stabilising Techniques*, (Sydney, Australia: New South Wales Institute of Technology, 1978), 201–219.

38. A. Di Donna, A. Ferrari, and L. Laloui, "Experimental Investigations of the Soil–Concrete Interface: Physical Mechanisms, Cyclic Mobilization, and Behaviour at Different Temperatures," *Canadian Geotechnical Journal* 53, no. 4 (2016): 659–672.

39. K. Roscoe and J. Burland, *On the Generalized Stress-Strain Behaviour of Wet Clay* (UK: Cambridge University Press, 1968).

40. F. E. Richart, J. R. Hall, and R. D. Woods, *Vibrations of Soils and Foundations* (Upper Saddle River, NJ: Prentice Hall, 1970).

41. Z. Y. Yin, Z. X. Wu, and P. Y. Hicher, "Modeling Monotonic and Cyclic Behavior of Granular Materials by Exponential Constitutive Function," *Journal of Engineering Mechanics* 144, no. 4 (2018): 04018014, https://doi.org/10.1061/(ASCE)EM.1943-7889.0001437.

42. Z. Y. Yin, C. S. Chang, and P. Y. Hicher, "Micromechanical Modelling for Effect of Inherent Anisotropy on Cyclic Behaviour of Sand," *International Journal of Solids and Structures* 47, no. 14–15 (2010): 1933–1951, https://doi.org/10.1016/j.ijsolstr.2010.03.028.

43. I. Einav, "Breakage Mechanics—Part I: Theory," *Journal of the Mechanics and Physics of Solids* 55, no. 6 (2007): 1274–1297, https://doi.org/10.1016/j.jmps.2006.11.003.

44. Y. F. Jin, Z. Y. Yin, Z. X. Wu, and A. Daouadji, "Numerical Modeling of Pile Penetration in Silica Sands Considering the Effect of Grain Breakage," *Finite Elements in Analysis and Design* 144 (2018): 15–29, https://doi.org/10.1016/j.finel.2018.02.003.

45. Z. Y. Yin and C. S. Chang, "Stress–Dilatancy Behavior for Sand Under Loading and Unloading Conditions," *International Journal for Numerical and Analytical Methods in Geomechanics* 37, no. 8 (2013): 855–870, https://doi.org/10.1002/nag.1125.

46. B. O. Hardin, "Crushing of Soil Particles," *Journal of Geotechnical Engineering* 111, no. 10 (1985): 1177–1192, https://doi.org/10.1061/(ASCE)0733-9410(1985)111:10(1177).

47. G. Zhang and J. M. Zhang, "Monotonic and Cyclic Tests of Interface Between Structure and Gravelly Soil," *Soils and Foundations* 46, no. 4 (2006): 505–518, https://doi.org/10.3208/sandf.46.505.

48. K. Fakharian, "Three-Dimensional Monotonic and Cyclic Behavior of Sand-Steel Interfaces: Testing and Modeling" (PhD thesis, University of Ottawa, 1996).

49. N. Hansen and A. Ostermeier, "Adapting Arbitrary Normal Mutation Distributions in Evolution Strategies: The Covariance Matrix Adaptation," in *Proceedings of the IEEE Conference on Evolutionary Computation* (Nagoya: IEEE, 1996), 312–317.

50. M. Zeghal and T. B. Edil, "Soil Structure Interaction Analysis: Modeling the Interface," *Canadian Geotechnical Journal* 39, no. 3 (2002): 620–628, https://doi.org/10.1139/T02-016.

51. W. Hou, "Research on Monotonic and Cyclic Behavior and Constitutive Model of Three-Dimensional Soil–Structure Interface" (PhD thesis, Tsinghua University, 2008).

52. R. H. Al-Douri and H. G. Poulos, "Static and Cyclic Direct Shear Tests on Carbonate Sands," *Geotechnical Testing Journal* 15, no. 2 (1992): 138–157.

10969853, 2024, 17, Downloaded from https://onlinelibrary.wiley.com/doi/10.1002/nag.3831 by HONG KONG POLYTECHNIC UNIVERSITY HU NG HOM, Wiley Online Library on [26/11/2024]. See the Terms and Conditions (https://onlinelibrary.wiley.com/terms-and-conditions) on Wiley Online Library for rules of use; OA articles are governed by the applicable Creative Commons License